# Assembly of tight junction belts by surface condensation and actin elongation

Alf Honigmann ( ✉ alf.honigmann@tu-dresden.de )

Technical University Dresden    https://orcid.org/0000-0003-0475-3790

Daxiao Sun

Tsinghua University

Xueping Zhao

Department of Mathematical Sciences, University of Nottingham

Tina Wiegand

Max Planck Institute of Molecular Cell Biology and Genetics

Giacomo Bartolucci

Max Planck Institute for the Physics of Complex Systems

Cecilie Martin-Lemaitre

Technical University Dresden

Stephan Grill

Max Planck Institute of Molecular Cell Biology and Genetics    https://orcid.org/0000-0002-2290-5826

Anthony Hyman

Max Planck Institute of Molecular Cell Biology and Genetics, 01307 Dresden    https://orcid.org/0000-0003-0851-704X

Christoph Weber

Faculty of Mathematics, Natural Sciences, and Materials Engineering: Institute of Physics, University of Augsburg

---

Article

Keywords:

Additional Declarations: There is **NO** Competing Interest.

---

# Title: Assembly of tight junction belts by surface condensation and actin elongation

**Authors:** Daxiao Sun[1,4†*], Xueping Zhao[2†], Tina Wiegand[1], Giacomo Bartolucci[3,5], Cecilie Martin-Lemaitre[4], Stephan W. Grill[1,6], Anthony A. Hyman[1,6], Christoph Weber[3*], Alf Honigmann[1,4,6,7*]

**Affiliations:**

[1]Max Planck Institute of Molecular Cell Biology and Genetics, Dresden, Germany.

[2]Department of Mathematical Sciences, University of Nottingham, Ningbo, China.

[3] Faculty of Mathematics, Natural Sciences, and Materials Engineering: Institute of Physics, University of Augsburg, Augsburg, Germany.

[4]Technische Universität Dresden, Biotechnologisches Zentrum, Center for Molecular and Cellular Bioengineering (CMCB), Dresden, Germany.

[5]Max Planck Institute for the Physics of Complex Systems, Dresden, Germany.

[6]Cluster of Excellence Physics of Life, TU Dresden, Dresden, Germany.

[7]Lead contact

†These authors contributed equally to this work.

*Corresponding authors: alf.honigmann@tu-dresden.de, christoph.weber@physik.uni-augsburg.de, dsun@mpi-cbg.de

20 **ABSTRACT**

Tight junctions play an essential role in sealing tissues, by forming belts of adhesion strands around cellular perimeters. The formation of a tight junction occurs into two steps, initiation at cell-cell contacts, and elongation around the perimeter. Recent work has shown that nucleation is governed by condensation of scaffold proteins. However, the mechanisms by which condensates are
25 spatially controlled to initiate at cell-cell contacts and elongate around cell perimeters remain unknown. Here, we combined cell biology, molecular reconstitution and thermodynamic modelling to show that belt formation is driven by a surface phase transition coupled to actin polymerization. Adhesion receptor oligomerization provides the signal for local surface condensation of ZO proteins. Surface condensates directly facilitate actin polymerization and
30 filament bundling, which drives elongation of receptor-ZO-actin condensates into a junctional belt. We conclude that surface phase transitions provide a robust mechanism to locally control the position and shape of protein condensates.

**INTRODUCTION**

Tight junctions are adhesion complexes that control the paracellular flux of solutes across tissues
35 [1-3]. The super-molecular structure of tight junctions is constructed from adhesion receptors of the claudin (CLDN) family, which form intercellular adhesion strands that act as diffusion barriers, and Zonula occludens (ZO) scaffold proteins which connect the receptors to the cytoskeleton [1]. Assembly of junctions is initiated by condensation of cytosolic scaffold ZO proteins at cell-cell contact sites that over time elongate and fuse around the apical cell perimeters into a continuous
40 belt which seals the tissue [4-6]. How cells spatially control condensation at cell-cell contacts and how the condensates are reshaped into closed belts has remained unclear.

The formation of protein condensates in the cytoplasm [7-9] and nucleoplasm [10,11] can be governed by thermodynamics [12]. Formation of condensates via phase separation requires protein
45 concentrations above the bulk saturation concentration [13]. However, on membrane surfaces condensate formation has been observed even far below bulk saturation [14-16], which suggests distinct phase transitions at the surface in comparison to the bulk. Surface phase transitions [17] including the prewetting transition have been originally predicted by Cahn [18] and have been found to be close to the saturation concentration in experimental polymeric systems [19-21]. However, a
50 recent theoretical study found that phase transitions can occur far below saturation if molecules can bind to the surface [22]. Indeed, a prewetting surface phase transition was proposed as a mechanism for condensation of transcription factors binding to DNA surfaces [23, 24]. How surface phase transitions are spatially controlled on biological membranes is not well understood.

55 In this work, we established how cells can induce a surface phase transition specifically at cell-cell contact regions and how subsequent interactions of surface condensates with the cytoskeleton drive its active remodeling into an elongated and functional tight junction belt.

## RESULTS

### Reconstitution of ZO1 membrane binding and surface condensation

To explore the mechanism of formation and maturation of junctional condensates into a belt structure, we reconstituted the tight junction assembly pathway on model membranes from purified components focusing on the intracellular components of the junction (Figure 1A), which comprise the cytoplasmic tails of adhesion receptors (CLDN2, JAM-A, CDH1, CRB3), the scaffold proteins (ZO1-3), adapter proteins (CGN, AFDN, PAR3) and the cytoskeleton (Actin) (Fig. S1, A and B). Initially, we aimed at characterizing the interactions of the main scaffold protein ZO1 to the strand forming receptor CLDN2 (Fig. 1A). We prepared fluorescently labeled C-terminal tails of CLDN2 containing the PDZ-binding motif for ZO1 and an N-terminal His-tag that allowed its attachment to $Ni^{2+}$-containing supported lipid bilayer (Fig. 1B) [14, 15]. During cell-cell adhesion CLDN receptors are known to oligomerize [25, 26]. To mimic different oligomerization states of the CLDN2 receptor, we attached GCN4 and ySMF domains that assemble into stable tetramers or 14-mers, respectively [27, 28]. This setup allowed us to systematically titrate receptor surface density and ZO1 bulk concentration to characterize binding and condensate formation.

In our vitro reconstitution setup, ZO1 condensates formed at concentrations larger than $c_{sat} = 11$ µM in solution (Fig. 1C), which is close to the cytoplasmic saturation concentration measured in epithelial cells [4]. The physiological concentration of ZO1 in the cytoplasm $c_{cyto} = 690$ nM is more than an order of magnitude lower than this bulk saturation concentration [4]. Thus, at physiological ZO1 concentration, condensates cannot spontaneously form in solution. However, we found that at these subsaturated conditions ZO1 proteins can bind to membranes containing monomeric, tetrameric and 14-meric CLDN2 receptors and thereby induce phase separation at the membrane surface (Fig.1, D-F). In absence of ZO1, monomeric and oligomeric receptors were homogeneously distributed and diffused quickly, e.g. molecules showed full recovery within seconds (Fig. S1, C to E). While ZO1 binding to monomeric receptors was homogeneous, binding of ZO1 to tetrameric and 14-meric receptors induced formation of phase separated condensates on the membrane surface (Fig. 1D). These surface condensates were not only strongly enriched in ZO1 but also dense in receptors compared to the coexisting dilute membrane phase. Imaging the dynamics of surface condensates showed initial coarsening and fusion of condensates on a timescale of 10 min indicating liquid-like properties (Fig. S2, Movie S1). However, over time the dynamics slowed down and condensates size typically saturated in the micrometer range (Fig. S3A). FRAP analysis showed partial exchange of ZO1 from the bulk but little diffusion in 2D (Fig. S3B), which is consistent with measurements at junctions in live cells [4].

To determine if the ZO1 surface condensates consist of a 2D protein monolayer or further extend into the bulk, we quantified the height of the ZO1 condensates on top of the membrane using atomic force microscopy (AFM) (Fig. 1G). AFM imaging revealed an average condensate height of 16 nm with respect to the membrane, which was largely independent of receptor surface density indicating that the structure of the condensed phase is stable over a large concentration range (Fig.

1H). Diffusion measurements of ZO1 in solution using fluorescence correlation spectroscopy showed a hydrodynamic diameter of 18 nm for a ZO1 dimer (Fig. 1I). Together, these measurements are consistent with ZO1 undergoing a surface phase transition into a condensed monolayer induced by binding to oligomerized adhesion receptors at subsaturated bulk concentrations.

**Receptor oligomerization induces robust surface condensation far below bulk saturation**

To understand how ZO1 surface binding and receptor oligomerization control surface phase separation, we developed a non-equilibrium thermodynamic model (Fig. 2A). In this model, scaffold proteins in the bulk solvent can bind to receptors in the membrane composed of lipids. Accounting explicitly for the receptors bound to scaffold proteins, the minimal model corresponds to a ternary mixture in the membrane and a binary model in the bulk. We describe the interactions among all components in bulk, membrane and between bulk and membrane using a Flory-Huggins free energy; detail see SI Theory. The model can be reduced to two unknown parameters, the dilute receptor binding affinity $\Omega$ and the interaction parameter $\chi$ characterizing the interactions among ZO1 proteins that are bound to receptors. Both parameters were obtained by fitting the model at equilibrium to experimental measurements of membrane bound ZO1 proteins as a function of receptor concentration and bulk ZO1 concentration (Fig. 2, B and D).

Despite the minimal nature of the model, we found very good agreement between the model and the experimental measurements. In particular, the model recapitulated the experimental ZO1 and receptor (14-mer) concentrations at which surface condensates appear as well as the concentrations in the condensed and dilute phases (Fig. 2, B to E). Consistent with the experimental data, the model predicted a jump in the difference in ZO1 concentrations between condensates and their surrounding dilute phase. To compare the dynamics of surface condensation and growth, we chose the kinetic parameters of the model in accordance with the FRAP studies of surface condensates (Fig. S3B). In agreement with experiments, we found that above the critical concentrations surface condensates form quickly but then transition to very slow coarsening kinetics (Fig.S3A, movie S1). This slow-down is caused by depletion of receptors in the dilute phase due to co-condensation of receptors and scaffold proteins, which effectively decreases ripening fluxes among surface condensates (Fig. 2, C and E). Taken together, the model suggests that ZO1 binding to oligomeric receptors triggers a discontinuous surface phase transition at the membrane.

After successfully calibrating the model, we analyzed how the oligomerization state of the receptor affects the surface phase transition. Fitting our model to the experimental data of both receptor states (Fig. 2, B and D and Fig. S3, C, and D), we determined the change in receptor binding affinity $\Omega$ and self-interaction parameter $\chi$ of receptor bound to ZO1 for monomeric and 14-meric receptors (definitions, see SI Theory Section G). The key finding is that the binding affinity of the 14-meric receptor to ZO1 is much stronger compared to the monomeric receptor (Fig. 2F). We found that the lower binding affinity of the monomer is dominantly caused by a reduced binding

4

fraction, i.e., only a small fraction of monomer receptors can bind to ZO1; a mechanism previously reported in Ref. [29]. Moreover, from the fits, we obtained that the bound ZO1-14-mer complexes strongly attract each other, i.e., they have a positive self-interaction parameter (Fig. 2F). While the fitted self-interaction of the ZO1-monomer complex was lower compared to the 14mer, a wide range of self-interaction parameters fitted the experimental data equally well (Fig. 2F, green shade), indicating that in the low affinity binding regime of the monomer receptor self-interactions at the surface play a minor role (see SI Theory Fig.3(a) and its related discussion). In summary, our results suggest that receptor oligomerization favors surface phase separation via two synergistic mechanisms. Increasing the binding affinity ($\Omega$) leads to a higher surface concentration of ZO1 at constant bulk concentration. While at the same time the self-interaction of the ZO1-receptor complex ($\chi$) lowers the saturation concentration required for membrane phase separation. Using the fitted parameters, we predicted the phase diagram for the monomeric and 14-meric receptors, which showed that there is no surface phase transition for monomeric receptors even for higher ZO1 concentrations, while there is a large region of surface phase separation for the 14-meric receptors (Fig. 2, G and H and Fig. S3, E and F). Based on the agreements between experiments and our thermodynamic model, we conclude that a surface phase transition underlies the formation of ZO1-rich surface condensation on membrane surfaces. The surface phase transition is controlled by the receptor's oligomerization state, suggesting cell adhesion-induced oligomerization could act as the key switch for ZO1 surface condensation at cell-cell contacts.

**Selective sorting of tight junction components by ZO1 surface condensates**

To study the relevance of surface condensates for tight junction assembly, we further increased the molecular complexity of our *in vitro* reconstitution (Fig. 3A). First, we asked whether ZO1 surface condensates can partition membrane receptors belonging to the adherens junction (CDH1), the tight junction (JAM-A) and the apical membrane (CRB3) (Fig. 3B). Before addition of ZO1, the intracellular domains of all receptors were well mixed on supported membranes (Fig. 3C). As before, addition of ZO1 initiated condensation of dense CLDN2-ZO1 domains. We found that the IC-domain of the tight junction receptor JAM-A was 2-fold enriched in the dense ZO1 phase (Fig. 3D). This is in line with JAM-A binding to ZO1 via PDZ2, which is independent of CLDN binding via PDZ1 [30] and suggests that ZO1 can simultaneously bind and crosslink different membrane receptors via its array of PDZ domains [31]. The adherens junction receptor CDH1 was evenly distributed between the dense and dilute phase indicating that there are no direct interactions with ZO1(Fig. 3, C and D). Surprisingly, we found that the ICD of the apical polarity receptor CRB3 was excluded from the ZO1 condensates, suggesting that segregation of apical and junctional proteins can be facilitated by condensation of ZO1 (Fig. 3, C and D). Thus, surface condensates could be an auxiliary mechanism in addition to apical polarization ensuring that cell-cell contacts are cleared from apical proteins to facilitate junction formation [32-34].

In addition to membrane receptors, we investigated the recruitment of cytosolic scaffold and adapter proteins (Fig. 3B). As predicted by our previous work studying ZO1 condensation in

solution [4], we found that the two ZO1 homologues ZO2 and ZO3 strongly partitioned in ZO1 surface condensates. The ZO1 binding proteins CGN, AFDN and PAR3 also became significantly enriched in the condensed phase, while the control protein mCherry showed neutral partitioning (Fig. 3, E and F). Together, these results established that ZO1 surface condensation drives sorting of key junctional components such as adhesion receptors and adapter proteins required for tight junction assembly into concentrated membrane domains which exclude the apical polarity proteins. While the colocalization of junctional proteins and the segregation of apical proteins *in vitro*, recapitulated to some degree the molecular organization of mature junctions in cells [1], the overall distribution and shape of the surface condensates was not changed and remained in a state that matched isolated condensates during the initial phase of junction assembly [4].

**Local actin polymerization drives surface condensates elongation**

To understand how nascent ZO1 surface condensates are reorganized into a belt structure resembling the structure of tight junctions, we investigated the interplay of the condensates with the actin cytoskeleton (Fig. 4A). Mature tight junctions are surrounded by a sub-apical belt of filamentous actin and perturbations of the actin cortex have been shown to disrupt junction structure and induce opening of the *trans*-epithelial barrier [35, 36]. Actin elongation is evident to correlate strongly with tight junction belt formation in MDCK II cells (Fig. S4). The junctional scaffold proteins ZO1, ZO2, CGN and AFDN contain actin-binding-domains (ABD), which have been suggested to provide the connection between the membrane receptors and the actin cortex [31, 35]. However, how actin binding is mechanistically related to junction formation is poorly understood. We first measured actin polymerization in the presence of 200 nM ZO1 in solution using G-actin labeled with pyrene (Fig. 4B). We found no significant influence of ZO1 on actin polymerization in solution, while a positive control (WASP+Arp2/3) showed strong increase (Fig. 4B). Next, we added fluorescently labeled G-actin to ZO1-CLDN2 membrane condensates. Under these conditions, actin was sequestered to surface condensates and rapidly polymerized into a membrane bound network (Fig.4, A and C, and movie S2). While no actin polymerization was observed on membranes without surface bound ZO1 or receptors (Fig. S5, C and D). Strikingly, actin polymerization induced reshaping of isolated condensates into a connected strand network with ZO1 and CLDN2 colocalizing with actin fibers (Fig. 4A). During the reshaping process ZO1 and CLDN2 surface concentrations remained constant while actin concentrations increased monotonically (Fig 4C). The initial elongation rate of the actin-condensates was $0.5 \pm 0.1$ µm/min (Fig. 4D), which is close to previously determined polymerization rates of single actin fibers [37]. Over time, actin filaments formed bundles by polymerization of new filaments along existing fibers (Fig. 4, E and F, and movie S3). Repeating the same experiment with a ZO1 mutant lacking the actin-binding-domain failed to induce actin polymerization (Fig. 4, G and H), despite similar surface phase separation properties of the ΔABR mutant as WT-ZO1 (Fig. S5, A and B). Quantification showed that actin became 5-fold enriched into WT-condensates while the ZO1-ΔABR was still able to enrich actin it was 2-fold reduced (Fig. 4I). In addition, comparing actin

6

recruitment to non-phase separated ZO1 bound to monomeric receptors on the membrane, showed that both actin polymerization and bundling were significantly reduced (Fig. S5, E and F).

220    Together, the results show that surface condensation of ZO1-CLDN2 is sufficient to sequester actin from solution and induce polymerization in an ZO1-ABR dependent manner (Fig. 4J). This suggests that the combination of weak actin binding affinity of ZO1 [36] together with the high density of actin binding sites in the surface condensates, provides robust spatiotemporal control for the assembly of an actin cortex at nascent cell-cell adhesion sites. In addition, the liquid-like

225    material properties of the condensed phase enable its spreading along the growing actin filaments, which results in the formation of continuous CLDN2-ZO1-Actin strands resembling the molecular organization of the tight junction belt. Interestingly, during the formation of the reconstituted junctional strands actin filaments grow as bundles (Fig. 4, E and F). Actin bundling, in contrast to branching, leads to elongation of condensates along a line and connects the condensates into a

230    sparse network with both its connectivity and complexity are constrained by the initial condensate density (Fig. S6). Thus, bundling could be an important feature of ZO1 condensates that promotes formation of a narrow subapical tight junction belt and prevents ectopic expansion of the tight junction into the lateral membrane domain.

235    Finally, we compared our *in vitro* reconstitution results to actin dependent tight junction assembly in epithelial tissue culture. To this end we prepared an MDCKII cell line that allowed us to follow the dynamics of endogenous ZO1 (NeonGreen tagged), and F-actin (Utrophin labeled) during junction assembly after perturbations via actin depolymerization by Latrunculin-A (LatA) or calcium depletion [4, 38]. In confluent MDCK monolayers ZO1 and F-actin colocalized at the TJ-belt

240    (Fig. 5A). Addition of 1 µM LatA let to rapid breakage of the TJ-belt and induced formation of condensates at the cell-cell interface resembling the initial ZO1 surface condensates in our *in vitro* experiments. Wash out of LatA induced actin polymerization and reformation of the junctional belt (Fig. 5B). Similar to our *in vitro* experiments, actin extended together with ZO1 condensates and connected single condensates into a continuous belt. Repeating these experiments using a

245    Calcium switch perturbation to reassemble junctions, resulted in similar behavior (Fig. 5B). Comparison of the elongation rates of junctional condensates quantified in MDCK tissue after LatA and Calcium switch with the elongation rates of our *in vitro* reconstitution assay showed a striking agreement (Fig. 5C). These results suggests that actin polymerization is the rate limiting process for tight junction belt elongation.

250

**DISCUSSION**

To summarize, we reconstituted the self-assembly of the intracellular part of the tight junction belt in an *in vitro* system, which enabled control of the concentrations of the components, quantification of molecular interactions, and observation of emergent behavior in ways that are

255    difficult to achieve using intact tissue. Combining the experimental results with thermodynamic

modeling, we found that a surface phase transition is triggered when cytoplasmic ZO1 binds to oligomeric adhesion receptors in the membrane. Exploring the coupling between bulk and surface interactions, revealed that surface condensation is largely independent of the cytoplasmic concentration of ZO1 and is rather controlled by receptor concentration and oligomerization. Thus, the interactions are tuned such that condensation in the bulk is suppressed due to sub-saturation but condensation at the membrane can be locally triggered by receptor enrichment and oligomerization, which are both occurring at cell-cell contact sites [39, 40]. We suggest that this mechanism provides robust spatiotemporal control to couple extracellular adhesion signals to intracellular assembly of the tight junction scaffold and possibly other adhesion junctions [16, 41].

Akin to other membrane condensates [14-16], we found that ZO1 condensation can create an environment that facilitates local biochemical reactions. ZO1 condensates enriched key junctional components, excluded apical proteins and facilitate actin polymerization and filament bundling. ZO1 condensation mediated actin polymerization drove a morphological transition from isolated domains into a continuous network of receptor-ZO1-actin strands. This reconstituted transition was remarkably similar in terms of morphology and kinetics to the junction assembly process in cells. While to create the junctional belt in cells additional mechanism will be required to align the elongating junctional condensates along the apical interface [42], our results suggest that a key driver for the elongation itself is the interplay between local actin polymerization and the cohesive forces of the ZO1 condensate. In contrast to other membrane condensates that interact with or nucleate actin filaments [14, 15], low affinity actin binding is directly inbuilt into the main scaffolder ZO1, which provides direct coupling between the surface phase transition and actin nucleation without partitioning of other actin nucleators. However, there are many additional actin binding proteins recruited to the junctional condensates, which may add robustness to system [43] and/or provide additional functions such as mechano-sensing [44, 45]. In addition to the actin dependent mechanism uncovered in this work, it will be important to understand how ZO1 condensates relate to the polymerization of Claudin receptors, which form the actual diffusion barrier.

More generally, our work shows how cells control and exploit the collective properties of protein condensates to actively assemble and shape complex biological structures. Recent examples have shown that interactions of protein condensates with biological surfaces such as DNA, cytoskeletal filaments or lipid membranes can drive mesoscale shape changes such as DNA compaction, cortex formation and membrane folding and budding [24, 46, 47]. Here we uncovered how cells convert punctual extracellular adhesion cues into continuous tight junction belts by exploiting surface phase transitions coupled to actin polymerization (Fig. 5D). We envision that our reconstitution platform in combination with our thermodynamic model will provide a template to uncover the assembly mechanism of other adhesion complexes and surface coupled cellular structures in general.

8

**METHODS**

The conducted research complies with all relevant ethical regulations. All studies were conducted according to the guidelines from the Academic Integrity and Ethics Committee of Max Planck Institute of Molecular Cell Biology and Genetics (MPI-CBG) and Technische Universität Dresden (TUD).

**Reagents and plasmids**

Protease inhibitor cocktail (Product No. 05056489001) was from Roche. Instant Blue Coomassie protein Stain (Product No. ab119211) was from Abcam. NuPAGE 4-14% Bis-Tris Gel (Product No. NP0322BOX) and Novex 10-20% Tricine Gel (Product No. EC66255BOX) were from Invitrogen. Benzonase, 3C protease, and mGFP were from the MPI-CBG facility. Latrunculin A (Product No. BML-T119-0100) was from ENZO. DyLight 550 NHS Ester (Product No. 62262), DyLight 650 NHS Ester (Product No. 62265), and Alexa647-maleimide (Product No. A20347) were from Thermo Scientific. SiR-SNAP (Product No. S9102S) was from NEB. Janelia Fluor HaloTag Ligand 646 (Product No. GA1120) was from Promega. Alexa Fluor 594 phalloidin (Product No. A12381) was from Life Technologies. Phospholipids including POPC (Product No. 850457), DGS-NTA(Ni) (Product No. 790404), PEG5000PE (Product No. 880230) and Rhodamine-PE (Product No. 810150) were from Avanti.

The coding sequence of ZO1 (human) and ZO1-deltaABR (human) was synthesized and cloned into a pOCC119 vector (MPI-CBG vector list) with a His-MBP tag for affinity purification and mGFP tag for visualization. The coding sequence of ZO1 (human), ZO2 (human), ZO3 (human), Cingulin (human), Afadin (human), and PAR3 (human) were synthesized and cloned into a pOCC216 vector (MPI-CBG vector list) with a His-MBP tag for affinity purification and mCherry tag for visualization. The coding sequence of CLDN2 C terminal (human) recombinant with a SNAP and JAM-A C terminal (dog) are synthesized and cloned into a pOCC39 vector (MPI-CBG vector list) with a His10 tag for affinity purification. The coding sequence of CLDN2 C terminal (human) recombinant with GCN4 or ySMF domains was synthesized and cloned into a pOCC221 vector (MPI-CBG vector list) with a His6 tag for affinity purification. The coding sequence of CDH1 (human) and CRB3 (human) was synthesized and cloned into a pOCC214 vector (MPI-CBG vector list) with a His6 tag for affinity purification and mCherry tag for visualization.

**Cell culture**

We used *Escherichia coli* Rosetta cells and SF9-ESF *S. Frugiperda* cells for recombinant protein purification. The *Escherichia coli* Rosetta cells were cultured in the LB medium supplemented with necessary antibiotics. The SF9-ESF *S. Frugiperda* cells were cultured with ESF 921 Insect Cell Culture Medium at 27℃. MDCK-II cells were cultured in DMEM with 1 g/L glucose, supplemented with 5% FBS, 1% non-essential amino acids at 37℃ with 5% $CO_2$.

**Generation of monomeric, tetrameric, and 14-meric receptors**

We used the last 7 amino acids from the human CLDN2 C-terminal as the receptor for recruiting ZO1 protein to the membrane. To make the receptor easier to purify, we fused a SNAP-tag before

9

335    the 7 amino acids to get a recombinant protein SNAP-CLDN2-C7 (referred to as monomer) as a monomeric receptor. We used GCN4 and ySMF domains, which are known to form stable tetramer and 14-mer, to get recombinant proteins GCN4-CLDN2-C7 (referred to as tetramer) and ySMF-CLDN2-C7 (referred to as 14-mer) as tetrameric and 14-meric receptors.

**Protein expression and purification of scaffold and adapter proteins**

340    For ZO1, ZO2, ZO3, CGN, AFDN, and PAR3, we used insect cells to recombinantly express proteins using the baculovirus expression system. SF9-ESF *S. frugiperda* cells were infected with respective baculoviruses, and then cultured at 27 °C in ESF 921 insect cell culture medium supplemented with 2 % fetal bovine serum for 3 days. Cell pellets were then collected, washed,

345    and resuspended with a lysis buffer (20 mM Hepes, pH 7.4, 500 mM NaCl, 1 mM $MgCl_2$, 1 x protease inhibitor cocktail, 1x benzonase). Cell pellets were broken with LM20 Microfluidizer, 5,000 psi, 2 runs, and clarified by centrifugation at 17,000 g, at 4 °C, for 30 min. Proteins were then purified with metal ion affinity chromatography (Ni-NTA) resin (IMAC, 5 mL HiTrap Chelating, GE Healthcare), and followed by amylose resin (NEB). Finally, size exclusion

350    chromatography was performed with the Superose 6 column on AKTA pure FPLC system (GE). Proteins were collected, aliquoted, and frozen in liquid nitrogen and stored at -80 °C in 20 mM Hepes, pH 7.4, 500 mM NaCl, 1 mM DTT, and 5 % Glycerol. His and MBP tag was cleaved and removed with amylose resin before being used for respective assays.

**Protein expression and purification of receptor proteins**

355    For monomer, tetramer, 14-mer, mCherry-CDH1-IC, JAM-A-IC and mCherry-CRB3-IC, we used *Escherichia coli* Rosetta cells to recombinantly express proteins. Proteins were expressed in the *Escherichia coli* Rosetta cells in LB medium at 16 °C overnight and induced with 0.2 mM IPTG when $OD_{600}$ reached 0.6 - 0.8. All the following steps were carried out at 4 °C. Cell pellets were

360    collected, washed and resuspended with a lysis buffer (20 mM Hepes, pH 7.4, 500 mM NaCl, 1 mM $MgCl_2$, 1 x protease inhibitor cocktail, 1x benzonase). Cell pellets were broken with LM20 Microfluidizer, 20,000 psi, 2 runs, and clarified by centrifugation at 17,000 g, at 4 °C, for 30 min. Proteins were then purified with metal ion affinity chromatography (Ni-NTA) resin (IMAC, 5mL HiTrap Chelating, GE Healthcare) and followed by size exclusion chromatography with Superdex

365    200 increase 10/300 GL column on AKTA pure FPLC system (GE). Proteins were collected, aliquoted, and frozen in liquid nitrogen and stored at -80°C in 20mM Hepes, pH 7.4, 500 mM NaCl, 1 mM DTT, and 5 % Glycerol.

**Protein fluorescence labeling**

370    Monomer, tetramer, 14-mer, and JAM-A-IC were labeled with DyLight550 NHS Ester (Thermo Scientific, Product No.62265) or DyLight 650 NHS Ester (Thermo Scientific, Product No.62262) dye. Highly purified proteins were prepared in 0.05 M sodium borate buffer at pH 8.5 (Thermo Scientific BupH Borate Buffer Packs, Product No. 28384). DyLight NHS Ester dyes were dissolved in DMSO. When labeling the protein, the dye and protein were mixed at a molar ratio

375 of 1:1, and incubated at RT for 1hr. Free dye was removed from the protein by desalting columns (Thermo Scientific Zeba Spin Desalting Columns, Product No. 89882) with buffer containing 20 mM Hepes, pH 7.4, 500 mM NaCl, 1 mM DTT, 5% Glycerol. Fluorescence labeling efficiency was measured with Nanodrop 2000 (ThermoFisher). The labeled and unlabeled proteins were mixed to get a final stock of 5 % labeled.

380

**Microscopy**

FRAP, FCS, and confocal imaging were performed on a commercial confocal STED microscope (Abberior Instruments, Göttingen, Germany) with pulsed laser excitation (490 nm, 560 nm, 640 nm, 40MHz) and 60x water or 100x oil objectives (Olympus). MDCKII cells were imaged on a

385 Nikon spinning disk microscope with a 60x water objective and a living cell imaging system supplying $CO_2$ and heating.

**Fluorescence recovery after photobleaching (FRAP)**

Regions of interest (ROI) were bleached using a 405 nm diode with 1.5 mW with 100 µs pixel

390 dwell time. Pre-bleached and post-bleached images were acquired with 490 nm, 560 nm, and 640 nm laser with a frame rate of 1 s for 10 min. Recovery data were normalized to a reference ROI outside the bleached area. FRAP traces were evaluated and fitted in GraphPad Prism software.

**Fluorescence correlation spectroscopy (FCS)**

395 mGFP, 5 % DyLight 550 and 5% DyLight650 labeled 14-meric receptors were anchored to SLBs via His10/His6 tag and DGS-NTA(Ni) interaction and excited with 490 nm, 560 nm and 640 nm pulsed laser (Olympus 60x NA = 1.2 water objective). Fluorescence fluctuations were recorded with a time resolution of 500 ns for 10 s. Auto-correlation of the photon traces was performed in MATLAB using a multiple tau correlator. The resulting correlation curves were fitted according

400 to the standard 2D diffusion model including one triplet component using MTALAB (Elson, 2011). The mean particle number N was obtained from the fitting. mGFP and ZO1-mGFP were excited with a 490 nm laser in the bulk. The resulting correlation curves were fitted according to the standard 3D diffusion model including one triplet component using MTALAB (Elson, 2011). The comparison of brightness between the two molecules was calculated by the counts per

405 molecule.

*Calibration curve generations*

FCS was performed on SLBs functionalized with different amounts of mGFP, 14-mer-DyLight 650 and 14-mer-DyLight 550. Mean particle numbers were obtained from FCS fitting. Confocal images were taken for the SLBs functionalized with mGFP, 14-mer-DyLight 650, or 14-mer-

410 DyLight 550 for extracting the mean fluorescence intensity. The mean fluorescence intensity of mGFP was normalized to ZO1-mGFP by the brightness comparison obtained from FCS measurement in the bulk. Calibration curves were obtained by plotting mean particle numbers as a function of fluorescence mean intensity.

*Hydrodynamic radius ($R_h$) measurement*

415    FCS measurements were performed on mCherry and ZO1-mCherry proteins with a 560 nm pulsed laser under the same buffer condition to get the diffusion coefficient. $R_h$ of the globular protein mCherry protein is known as ~2.6 nm. The Stokes-Einstein equation was used to get the $R_h$ of ZO1-mCherry protein by plugging the diffusion coefficient and $R_h$ of mCherry proteins into it.

420    **3D phase separation assay and saturation concentration determination**
       MBP tag was cleaved by adding 3C proteases to ZO1-GFP-3C-MBP protein stock at RT for 3 hrs. Protein stock was then diluted to a 3D phase separation buffer (20 mM Hepes, pH 7.4, 150 mM NaCl) to a series of concentrations. Images were taken with a confocal microscope (Olympus 60x NA = 1.2 water objective) in a glass-bottomed 384-well plate that was pre-blocked with 1 mg/ml
425    BSA. Saturation concentration was determined by quantifying the concentration in the dilute phase with a calibration curve acquired with concentration without condensation.

       **Supported lipid bilayer (SLB) preparation**
       *Small unilamellar vesicle (SUV) preparation*
430    Phospholipids including POPC (Avanti, Product No. 850457), certain amounts of DGS-NTA(Ni) (Avanti, Product No. 790404), 0.1 % PEG5000PE (Avanti, Product No. 880230) and 0.1 % Rhodamine-PE (Avanti, Product No. 810150) were mixed in chloroform in glass bottles, and dried under vacuum for 2 hrs. 500 uL to 1 mL buffer (20 mM Hepes, pH 7.4, 150 mM NaCl and 10 mM MgCl$_2$) was added to the dried lipid film to make a final lipid concentration as 1 mM and
435    resuspended by shaking at a speed of 180 rpm, at 37 °C for 1 hr. The lipid mixture was then transferred to the Eppendorf tube and went through freeze-thaw for 15 runs until the lipid mixture became clear. The SUVs were further clarified by centrifugation at 17,000 g for 30 min and stored at 4 °C for use within one week.
       *SLBs generation*
440    Glass-bottomed 96-well plates (Greiner, Product No. 655891) were pre-cleaned with 2 % Hellmanex II overnight and 6 M NaOH for 30 min at RT twice. Before adding SUVs, wells were equilibrated with buffers (20 mM Hepes, pH 7.4, 150 mM NaCl, and 10 mM MgCl$_2$) for 5 min, and left a 60 uL buffer in the well. 20 uL 1 mM SUVs were added and incubated for 20 min. 20 uL 5 M NaCl was then added for another 20 min for the SUVs to further collapse on the glass
445    bottom. Excess SUVs were intensively washed away by pipetting in and out buffers (20 mM Hepes, pH 7.4, 150 mM NaCl, and 10 mM MgCl$_2$) 8 to 10 times. The quality of SLBs was checked by FRAP under a confocal microscope.

       **ZO1 Surface phase separation assay on SLBs**
450    SLBs with a certain amount of DGS-NTA(Ni) lipids were blocked with 1 mg/ml BSA for 30 min. 500 nM monomeric, tetrameric, or 14-meric receptors were added and incubated for 30 min. Excess receptors were washed away by pipetting in and out buffer (20 mM Hepes, pH 7.4, 150 mM NaCl and 10 mM MgCl$_2$) 8 to 10 times. The images of receptors on SLBs before adding ZO1 were taken with a confocal microscope and converted to number density with respective

12

455　calibration curves. The dynamics of receptors on SLBs before adding ZO1 were measured by FRAP. Certain amounts of ZO1-mGFP were added for 15 min to form ZO1 surface condensates. 3 images for each well were randomly taken under a confocal microscope. Time lapses were taken with a frame rate of 10 s for 15 min.

460　**Client protein partition assay on SLBs**

For the partition assay of cytosolic proteins including ZO2-mCherry, ZO3-mCherry, CGN-mCherry, AFDN-mCherry, PAR3-mCherry, and mCherry (used as a negative control), ZO1 surface condensates were formed by adding 100 nM ZO1 to membrane-bound 14-mer-DyLight 650 (680 molecules/$\mu m^2$) for 15 min. Images were taken after adding 100 nM client proteins to

465　ZO1 surface condensates for 15 min. 3 images for each well were randomly taken under a confocal microscope.

For the partition assay of receptor proteins including CDH1-IC, JAM-A-IC, and CRB3-IC. 14-mer receptor-DyLight 650 (50 nM protein was used for the incubation) and client receptors (500 nM protein was used for the incubation) were anchored to SLBs containing 8 % DGS-NTA(Ni).

470　Excess receptors were washed away by pipetting in and out buffer (20 mM Hepes, pH 7.4, 150 mM NaCl and 10 mM $MgCl_2$) 8 to 10 times. Receptors on SLBs before adding ZO1 were imaged with a confocal microscope and dynamically checked by FRAP. 100 nM ZO1 was added for 15 min to form ZO1 surface condensates.

Partition coefficients of client proteins into ZO1 surface condensates were quantified by measuring

475　the fluorescence intensity of client proteins inside ZO1 surface condensates and normalized to the fluorescence intensity of client proteins outside ZO1 surface condensates.

**Atomic force microscopy (AFM) imaging**

For characterizing the height of ZO1 surface condensates, we performed AFM topography

480　measurements at a JPK NanoWizard4 AFM (Bruker Nano GmbH, Germany). ZO1 surface condensates were prepared in 35 mm glass-bottomed dishes (MatTek Corporation, Product No. P35G-0.170-14-C). Images were acquired in JPK's "Q.I." mode (force mapping imaging) using "Biolever mini" cantilevers (BL-AC40TS-C2, Lot No. 840166, Olympus, Japan). Probes were calibrated before each measurement using the "contact-free" method implemented in the

485　"NanoWizard Control Software" (version 6.1, JPK Instruments, Germany). The setpoints for the measurements were chosen between 0.1 and 0.2 nN, z-lengths between 100 and 250 nm, and pixel times between 6 and 10 ms.

Image processing was carried out using JPK's "Data Processing" software (version 6.1, JPK Instruments, Berlin, Germany). Maps of "height (measured)" were leveled line by line by fitting a

490　first-order polynomial to the height values, only taking into account the substrate. Other than that, height maps were not subjected to further processing.

**Muscle actin purification and labeling**

Monomeric actin was purified from rabbit skeletal muscle acetone powder (Pel-freeze, USA, cat.
no: 41995) following standard protocols [48] and kept at 4 °C throughout handling.

A subset of depolymerized actin was labeled with either N-(1-Pyrenyl) iodoacetamide (Molecular
Probes, USA) or Alexa647-maleimide (Thermo Fischer Scientific, cat. no: A20347). Therefore
2.5 mL of the dialyzed solution were buffer exchanged with a PD-10 column (Cytiva, USA) into
DTT-free buffer (5 mM Tris-HCl pH 8, 0.2 mM ATP, 0.1 mM $CaCl_2$) and reacted at the equimolar
ratio with Alexa-647 maleimide for 2 hrs in the dark. Aggregates have been removed by
ultracentrifugation at 350 000 g for 20 min and actin in the supernatant was polymerized for 2 hrs
by addition of 10x KMEI buffer (500 mM KCL, 10 mM $MgCl_2$, 10 mM EGTA, 100 mM Imidazole
HCL, pH 7.0) and ATP to final concentrations 1x and 1 mM, respectively. Subsequently, actin
filaments were pelleted again by ultracentrifugation at 100,000 g for 2 hrs, washed, and
resuspended in 1.5 mL CaBuffer-G (2 mM Tris-HCl, pH 8.0, 0.2 mM ATP, 0.5 mM DTT, 1 mM
NaN3, 0.1 mM $CaCl_2$) by homogenizing 10x with a douncer. The labeled actin solution was
dialyzed against CaBuffer-G for 3 days to depolymerize actin. All actin solutions were filtered
through 0.22 µm PTFE filters, ultracentrifuged for 2 hrs at 100,000 g, and gel-filtered on a
superdex 200 column with CaBuffer-G. Only post-peak fractions were used for polymerization
assays to assure a monomeric solution. Unlabeled and pyrene-labeled actin was stored at 4 °C for
up to 4 weeks. Alexa647-labeled actin was flash-frozen with liquid nitrogen and stored at -80 °C.
On the day of the experiment, Alexa647-labeled actin was rapidly thawed by hand and clarified
by ultracentrifugation at 100,000 x g for 2 hrs at 4 °C using the top 75 % of the supernatant. Actin
concentrations were determined in a nanophotometer (NP80, Implen, USA) at 290 nm (38.5 µM
cm) and mixed to yield a 5 - 10 % labeled fraction.

**Actin-pyrene polymerization assay in bulk**

Actin assembly was monitored by pyrene fluorescence in 150 µL total reaction volume in 96 well
formats with a Spark 20M (Tecan) plate reader (top reading, λex = 365 nm, λem = 407 nm, every
10 s, 90 min total time, T = 25 °C). Ca-ATP-actin (5 % pyrene-labeled) was converted to Mg-
ATP-actin by incubation with 1/10th volume of 10x Mg exchange buffer (500 µM $MgCl_2$, 2 mM
EGTA) for 2 min at RT. Mg-ATP actin was then mixed at a final concentration of 2 µM with the
respective proteins (diluted to 1 µM in their buffer, final concentrations see Table 1 below) and
transferred in up to 12 rows of a 96 well plate (half area, µClear, black, Greiner Bio-one, cat. no.
675090). Using a multichannel pipette Mg buffer-G (2 mM Tris-HCl, pH 8.0, 0.2 mM ATP, 0.5
mM DTT) and 1/10th volume of 10x KMEI buffer (500 mM KCl, 10 mM $MgCl_2$, 10 mM EGTA,
100 mM Imidazole-HCL, pH 7.0) were added to actin in all wells simultaneously and the recording
was started within 10 s.

Table 1

| | C(start) in µM | C(final) in µM | V (uL) |
|---|---|---|---|
| Ca-ATP actin (5 % pyrene labeled) | 10 | 2 | 30.0 |

| | | | |
|---|---|---|---|
| 10x Mg exchange buffer | 10 | 1 | 3.0 |
| ZO1 | 2 | 0.2 | 15.0 |
| 10x KMEI buffer | 10 | 1 | 15.0 |
| Mg Buffer-G | | | 87 |
| V (total) | | | 150 |

530

**Actin polymerization assay on SLBs**

ZO1 surface condensates were prepared by adding 200 nM ZO1 to membranes functionalized with 14-mer-DyLight 550 or monomer-DyLight 550 receptors for 10 min in 50 µL total volume of actin polymerization buffer (2 mM Tris-HCl pH 8.0, 150 mM KCl, 10 mM $MgCl_2$, 0.2 mM ATP, 1 mM

535 EGTA) supplemented with ATP regeneration and oxygen scavenger systems [49]: phosphocreatine (10 mM), creatine phosphokinase (53 U/ml), pyranose oxidase (3.7 U/ml, Merck, cat. no. P4234), catalase (90 U/ml, Merck, cat. no. C40), 0.4 % glucose and 2mM 2-Mercaptoethanol.

Ca-ATP-actin (5 % AlexaFluor647-labeled) was converted to Mg-ATP-actin by incubation with 1/10th volume of 10x Mg exchange buffer (500 µM $MgCl_2$, 2 mM EGTA) for 2 min at RT. 15 ml

540 of 13 µM Mg-ATP actin were then added to reach a final concentration of 3 µM and confocal time-lapse images were recorded with a frame rate of 30 s for 1 hr. Additionally, images at random spots were taken 1 h after the addition of actin.

For determining the dependence of actin polymerization on the receptor densities, membranes functionalized with different amounts of 14-mer receptors were used. Membranes without a

545 receptor, without ZO1, or with ZO1-ΔABR were used as control. The length of ZO1 and actin networks were extracted with the plugin Skeleton in Fiji (https://fiji.sc/).

**Production of CLDN2 visualization cell lines and F-actin visualization cell lines**

CRISPR/Cas9 method was used to generate the N-terminal ZO1 NeonGreen (NG-ZO1) knock-in

550 cell line in MDCK II cells as described before (*4*). On top of this, a mammalian expression plasmid with an N-terminal SNAP-tag and the first 261 amino acids of human utrophin (an F-actin binding protein) or an N-terminal Halo-tag CLDN2, was transfected using Lipofectamine-2000. Stable transgenic cell lines were selected in the presence of geneticin (400 ug/mL). For visualizing the actin, SNAP-Utrophin stable expressing cell lines were labeled with 3 µM SNAP substrate (SiR-

555 SNAP, Product No. S9102S) for 30 min before imaging. Free SNAP substrate was washed away before imaging. For visualizing the CLDN2, Halo-CLDN2 stable expressing cell lines were fixed with 4% PFA, quenched with 200 mM Glycine, and then labeled with 200 nM Janelia Fluor HaloTag Ligand 646 (Promega, Product No. GA1120) for 1 hour. The free substrate was washed away before imaging.

### F-actin staining with Phalloidin

N-terminal ZO1 NeonGreen (NG-ZO1) knock-in and Halo-CLDN2 stable expressing MDCK II cell line was fixed with 4% PFA and quenched with 200 mM Glycine. Alexa Fluor 594 phalloidin (Life Technologies, Product No. A12381) was added as 1:500 to stain the F-actin for 1 hour. Free

dye was washed away before imaging.

### Latrunculin-A (LastA) switch assay

ZO1-NG knock-in, SNAP-Utrophin stable expressing MDCK II cells were cultured in full medium (DMEM with 1 g/L glucose, supplemented with 5% FBS, 1% non-essential amino acids) at 37 ˚C

with 5% $CO_2$ until they formed a confluent monolayer. For visualizing the actin, 3 µM SNAP substrates (SiR-SNAP, Product No. S9102S) were added for 30 min before imaging. Free SNAP substrate was washed away before imaging. 1 µM LatA was added for 30 min to disrupt the tight junction. LatA was then washed away. Time series images were taken under a Nikon spinning disk confocal every 80 s for 12 hrs to capture the elongation of tight junction belts after washing away

the LatA.

### Calcium switch assay

ZO1-NG knock-in, SNAP-Utrophin stable expressing MDCK II cells were cultured in full medium (DMEM with 1 g/L glucose, supplemented with 5% FBS, 1% non-essential amino acids) at 37 ˚C

with 5% $CO_2$ until they formed a confluent monolayer. Confluent MDCK II monolayer was switched to a calcium depletion medium (Gibco, Product No. 21068) for 18 hrs until the tight junction was completely disrupted. For visualizing the actin, 3 µM SNAP substrates (SiR-SNAP, Product No. S9102S) were added for 30 min before imaging. Free SNAP substrate was washed away before imaging. The full medium with calcium was then switched back. Time series images

were taken under a Nikon spinning disk confocal every 80 s for 12 hrs to capture the formation of tight junction belts.

### Statistics and reproducibility

Images were analyzed with FIJI (https://fiji.sc/) or MATLAB (Mathworks). Statistical details for

each experiment can be found in the figure legends and the corresponding methods. Data shown with error bars are presenting the standard deviation (SD).

### DATA AND CODE AVAILABILITY

This article includes all datasets generated or analyzed during this study.

### RESOURCE AVAILABILITY

Further information and request for resources and reagents should be directed to and will be fulfilled by the lead contact, Alf Honigmann (alf.honigmann@tu-dresden.de). All unique/stable

reagents generated in this study are available from the Lead Contact with a completed Materials Transfer Agreement.

## SUPPLEMENTARY MATERIALS

### MOVIES S1-S3

**Movie S1. ZO1 surface Condensation.** 1400 molecules/ $\mu m^2$ 14-mer receptors (labeled with 5% DyLight 650, Magenta) were anchored to DGS-NTA(Ni) containing lipid membranes. Images were taken every 10s for 15 min after adding 200 nM ZO1-mGFP (Green). ZO1 was gradually recruited to the membrane, and de-mixed to form a dense phase and a dilute phase. During this process, Ostwald ripening and fusion events happened to form surface condensates.

**Movie S2. Local actin polymerization.** 450 molecules/ $\mu m^2$ 14-mer receptor (labeled with DyLight 550, Magenta) was anchored to DGS-NTA(Ni) containing lipid membrane. 200 nM ZO1-GFP (Green) was added for 10 min to form ZO1 surface condensates. 3 $\mu M$ G-actin (labeled with 5% Alexa Fluor 647, Yellow) was added to ZO1 surface condensates. Images were taken every 30 s for 60 min. G-actin was recruited to ZO1 surface condensates, polymerized out and bundled. Actin bundles connected with each other to form a network. Simultaneously, ZO1 surface condensates spread on actin bundles to form a continuous receptor-ZO1-actin network.

**Movie S3. Local actin bundling.** Actin bundling during the time was quantified from movie S2. Actin polymerized from the ZO1 surface condensates as a single filament. New actin filaments grew on top of the F-actin filaments to form actin bundles.

### SUPPLEMENTARY INFORMATION ON THEORETICAL MODEL

A. Model for protein binding to receptors in a membrane

B. Thermodynamics and molecular interactions

C. Equilibrium thermodynamics

D. Binding fraction

E. Non-equilibrium thermodynamics with membrane binding

F. Parameter choices and parameters obtained from fitting to the experimental data

G. Derivation of dilute binding affinity given in Eq. (23)

H. Kinetics of membrane phase separation

References

635

640

**AUTHOR CONTRIBUTIONS**

645     A.H. and D.S. conceived the experimental part of the project. C.W. and X.Z. conceived the physical model. D.S. purified proteins and performed all experiments. X.Z. implemented and fitted the model. T.W. performed the actin polymerization assay in solution and helped with actin polymerization on SLBs. C.M. established stable MDCKII cell lines. D.S., A.H. and X.Z. analyzed the experimental data. A.H., C.W., D.S., X.Z and A.A.H. wrote the manuscript.

650

**DECLARE OF INTERESTS**

The authors declare no competing interests.

**FIGURES**
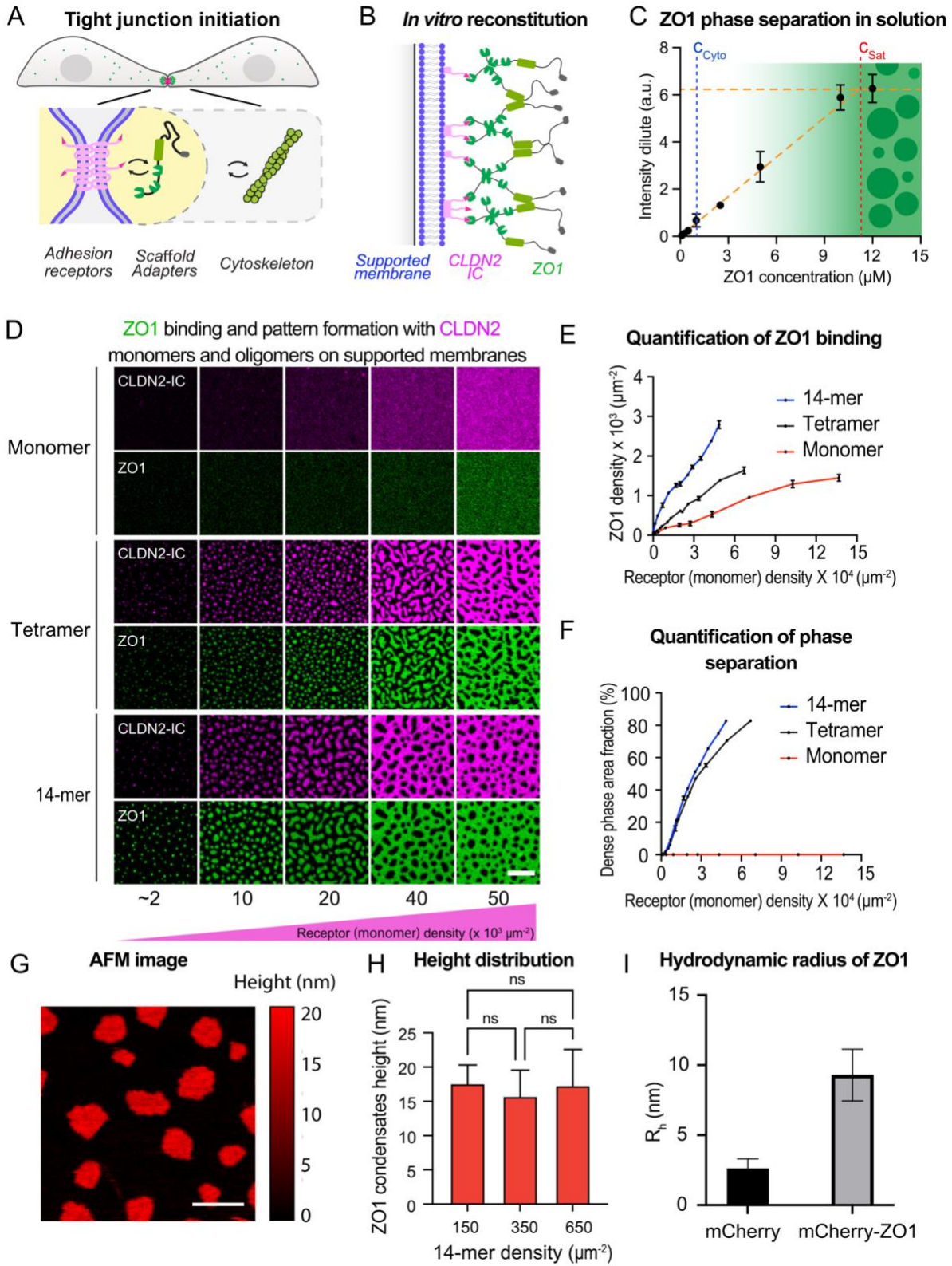
**Fig. 1. Receptor oligomerization drives ZO1 surface binding and condensation under physiological concentration.**

(A) Schematic of tight junction initiation with cell-cell contact in epithelial cells.

(B) Schematic of the reconstitution system with supported lipid bilayers (SLBs) and tight junction components.

(C) Saturation concentration of ZO1 ($C_{sat}$) in solution quantified by fluorescence intensity in dilute phase. Values shown are the mean ± SD from three independent experiments. The saturation concentration ($C_{sat}$) in the solution and cytosolic concentration ($C_{cyto}$) of ZO1 are annotated.

(D) Images of ZO1 surface condensates with increased receptor density of 14-mer, tetramer and monomer. Receptor densities annotated at the bottom indicate the number of monomeric receptors on the surface. 100 nM ZO1 was added to membrane-bound receptors for 15 min to form ZO1 surface condensates. Scale bar, 5µm.

(E) Quantification of ZO1 membrane binding from the images in (D). Values shown are the mean ± SD from three different views.

(F) Quantification of dense phase area fraction from the images in (D. Values shown are the mean ± SD from three different views.

(G) AFM images of ZO1 surface condensates. ZO1 membrane condensates were formed by adding 25 nM ZO1 to 650 molecules/ $µm^2$ membrane-bound 14-mer receptors for 15 min. Scale bar, 1µm.

(H) Quantification of surface height from AFM images with different 14-mer densities. ZO1 membrane condensates were formed by adding 100 nM ZO1 to different amounts of membrane-bound 14-mer receptors for 15 min. Values shown are the mean ± SD from three different views.

(I) Hydrodynamic radius ($R_h$) of mCherry and mCherry-ZO1 proteins from FCS measurement. Values shown are the mean ± SD from 9 independent measurements.
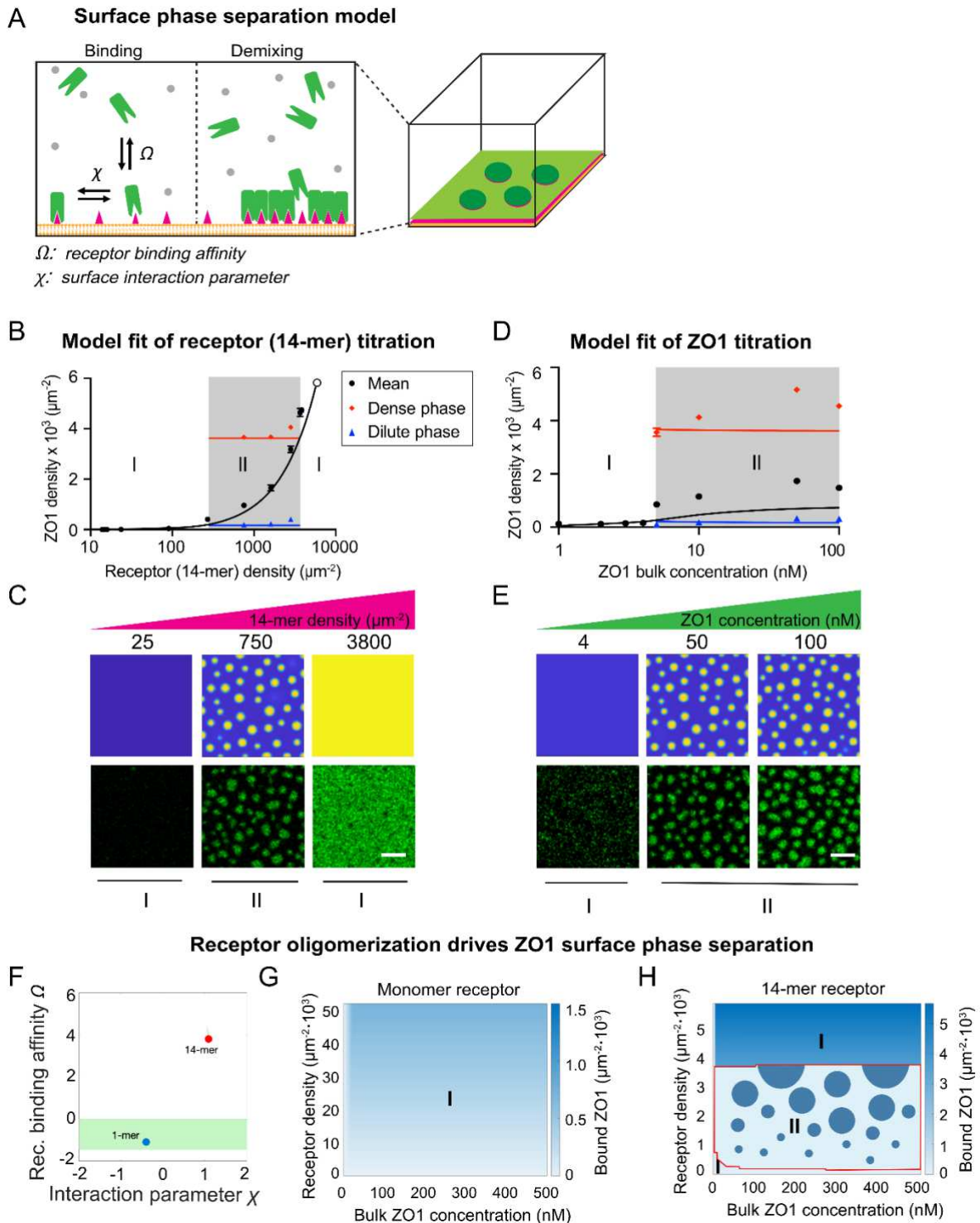
**Fig. 2. ZO1 membrane condensates form via surface phase separation under the sub-saturation regime.**

(A) Schematic of the surface phase separation model with specific receptor binding. Left shows the two free parameters the receptor binding affinity Ω, which controls how much ZO1 can

685   accumulate at the surface. And the surface interaction parameter χ, which contributes to the condensation of ZO1-receptor complexes.

(B) Model fitting of ZO1 density on whole membrane, in dense phase and in dilute phase when titrating the 14-mer receptor densities. Values shown are the mean ± SD from three different views.

(C) Up: Snapshots of ZO1 surface condensates from simulation when titrating the 14-mer receptor
690   density. Down: Images of ZO1 surface condensates from experiment when titrating the 14-mer receptor density. ZO1 surface condensates were formed by adding 50 nM ZO1 to the membrane functionalized with different amounts of 14-mer receptors. Scale bar, 2 µm.

(D) Model fitting of ZO1 density on whole membrane, in dense phase and in dilute phase when titrating the ZO1 bulk concentration. ZO1 surface condensates were formed by adding different
695   amounts of ZO1 to the membrane functionalized with 750 molecules/µm$^2$ 14-mer receptors. Scale bar, 2 µm.

(E) Up: Snapshots of ZO1 surface condensates from simulation when titrating the ZO1 bulk concentration. Down: Images of ZO1 surface condensates from experiment when titrating ZO1 bulk concentration. ZO1 surface condensates were formed by adding different amounts of ZO1 to
700   the membrane functionalized with 750 molecules/µm$^2$ 14-mer receptors. Scale bar, 2 µm.

(F) Binding affinity (Ω) and interaction parameter (χ) with monomer and 14-mer from the fitting. In the phase diagram, the area demarcated in light green represents all parameter sets that yield Mean Square Error (MSE) values less than or equal to 130% of the minimal error observed. This zone therefore indicates a level of performance close to optimal, within an acceptable threshold of
705   variability.

(G) Phase diagram of ZO1 membrane binding with monomer receptor on membrane from simulation. Phase I shows the regime with mixed surface and mixed bulk.

(H) Phase diagram of ZO1 membrane binding with 14-mer receptor on membrane from simulation. Different regimes are annotated. Phase I shows the regime with mixed surface and mixed bulk.
710   Phase II shows the regime with demixed surface and mixed bulk.
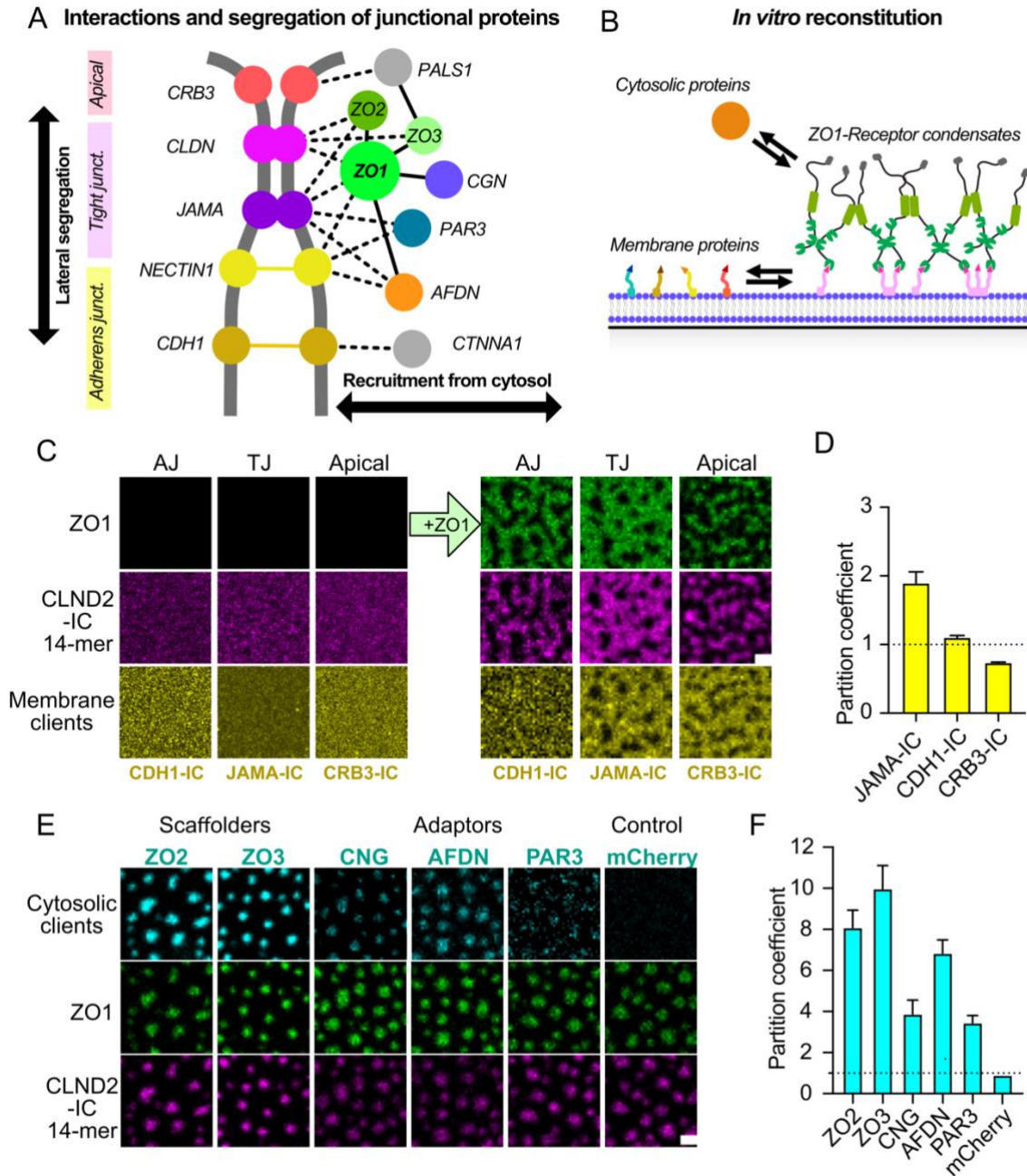
**Fig. 3. ZO1 surface condensates selectively enrich tight junction components.**

(A) Schematic of tight junction structures with indication of different tight junction components and non-tight junction components in lateral and apical.

(B) Schematic of partition assay with different cytosolic and membrane components.

(C) Left: Images of membrane functionalized with 14-mer together with JAM-A-IC, 14-mer together with E-Cad-IC, and 14-mer together with CRB3-IC. Right: Images of different receptors partitioned into or segregated with ZO1 surface condensates. ZO1 surface condensates were formed by adding 100 nM ZO1 for 15 min. Scale bar, 2 µm.

(D) Partition coefficient quantification of different receptors into ZO1 surface condensates from images in (C). Values shown are the mean ± SD from 3 different views.

(E) Images of cytosolic tight junction components partitioning into ZO1 surface condensates. mCherry protein was used as a negative control. ZO1 membrane condensates were formed by adding 100 nM ZO1 to 680 molecules/µm$^2$ membrane-bound 14-mer for 15 min. Images were taken after adding 100 nM client proteins to ZO1 surface condensates for 15 min. Scale bar, 2 µm.

(F) Partition coefficient quantification of cytosolic tight junction components into ZO1 surface condensates from images in (E). Values shown are the mean ± SD from 3 different views.
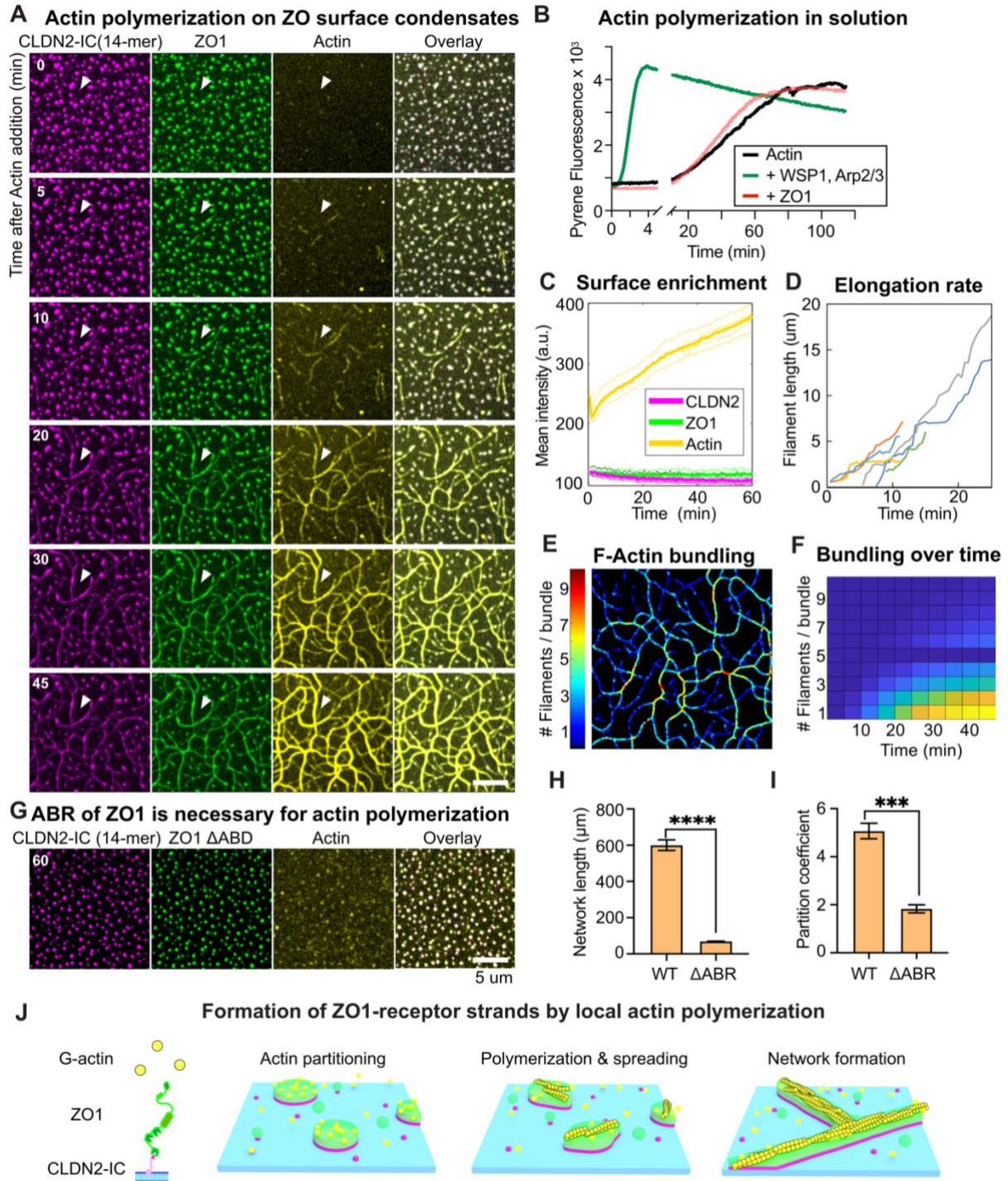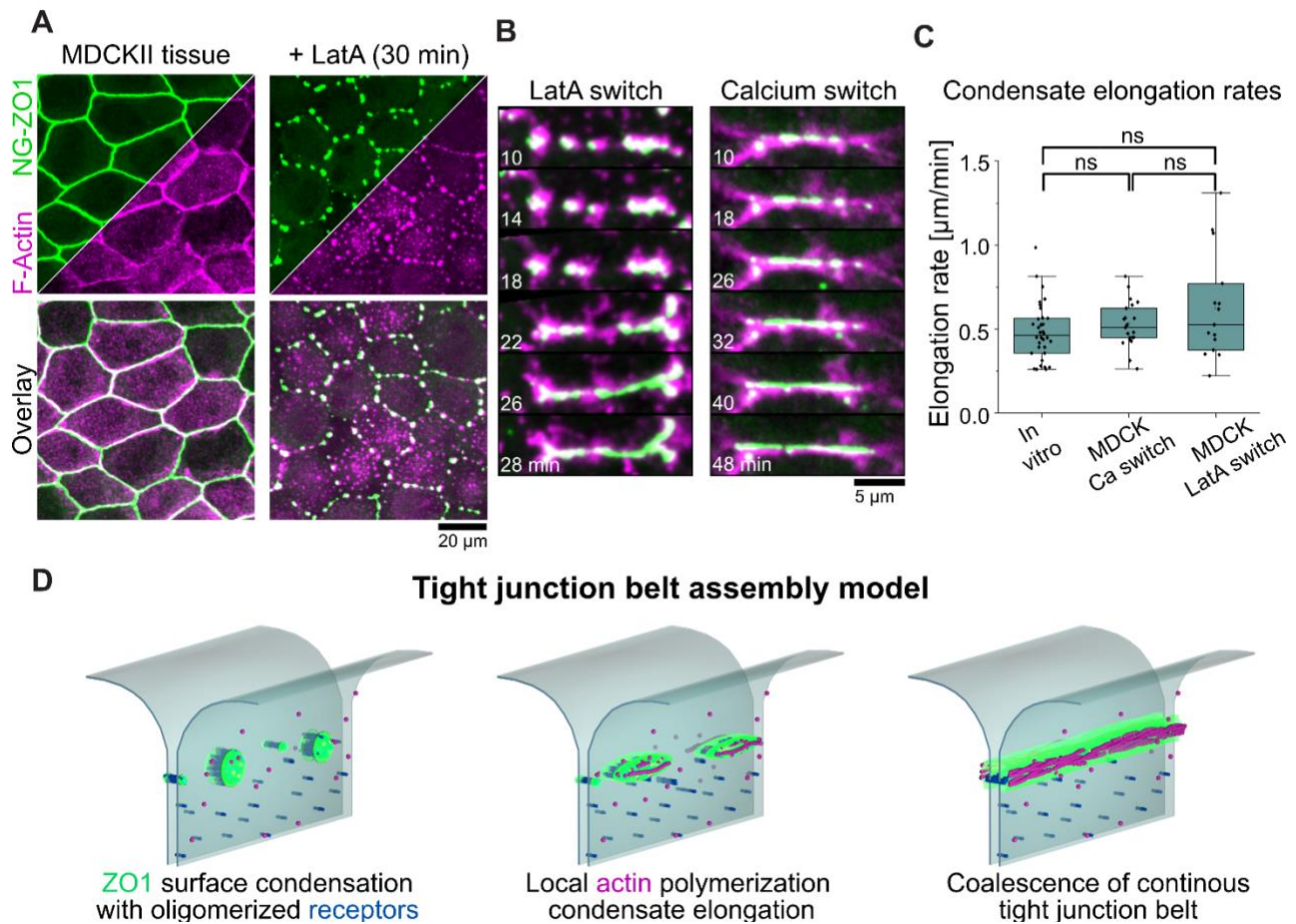
**Fig. 4. Local actin polymerization drives elongation of junctional condensates**.
(A) Time series of local actin polymerization and ZO1 surface condensates deformation. ZO1 surface condensates were formed by adding 200 nM ZO1 to 450 molecules/µm² membrane-bound 14-mer-DyLight 550 for 10min. Image series was taken after adding 3 uM G-actin-Alexa Fluor 647 to ZO1 membrane condensates every 30 s for 60 min. The white arrowhead indicates one

example of actin filament polymerization and ZO1 surface condensates spreading. Scale bar, 2 µm.

(B) Pyrene actin polymerization assay in tube with 200 nM ZO1 or 100 nM Arp2/3 and 100 nM WASP1.

(C) Quantification of ZO1, 14-mer receptor and actin fluorescence on membrane during time from the time series in (A).

(D) Quantification of actin filaments growth during time from the time series in (A).

(E) Color map of F-actin bundling degree after adding 3 uM G-actin-Alexa Fluor 647 for 60 min.

(F) F-actin bundling degree during time from the time series in (A).

(G) Actin local polymerization assay with ZO1-ΔABR surface condensates. ZO1-ΔABR surface condensates were formed by adding 200 nM ZO1-ΔABR protein to the membrane functionalized with 450 molecules/µm$^2$ 14-mer for 10 min. Images were taken after adding 3 uM G-actin-Alexa Fluor 647 for 60 min. Scale bar, 10 µm.

(H) Quantification of actin network length with ZO1 surface condensates formed with ZO1-WT and ZO1-ΔABR. Values shown are the mean ± SD from 3 different views. Unpaired t-test was performed to determine the significance of the difference. P = 0.0001.

(I) Partition coefficient of actin signal into the ZO1 surface condensates formed with ZO1-WT and ZO1-ΔABR. Values shown are the mean ± SD from 3 different views. Unpaired t-test was performed to determine the significance of the difference. P < 0.0001.

(J) Schematic of local actin polymerization, ZO1 surface condensates spreading and tight junction like network formation on membrane.

**Actin dependent condensate elongation and belt formation in MDCKII tissue**

**A**

MDCKII tissue | + LatA (30 min)

NG-ZO1
F-Actin
Overlay

20 μm

**B**

LatA switch | Calcium switch

10
14
18
22
26
28 min

10
18
26
32
40
48 min

5 μm

**C**

Condensate elongation rates

ns
ns | ns

**D**

**Tight junction belt assembly model**

ZO1 surface condensation
with oligomerized receptors

Local actin polymerization
condensate elongation

Coalescence of continous
tight junction belt

760

Figure 5. **Actin dependent elongation of junctional condensates in epithelial tissue**
(A) Colocalization of ZO1 and F-actin in confluent monolayers of MDCK cells. Endogenous ZO1
was visualized via fusion NeoGreen (NG). F-actin was visualized via the binding protein UtrCH
765    fused to a SNAP-tag and stained with SiR-SNAP. Addition of 1μM Latrunculin-A (LatA) induces
actin depolymerization and results in the formation of junction condensates enriched in ZO1 and
actin.
(B) Junction assembly assay using the same cell line described in (A). Left panel: LatA was wash
out and ZO1 and F-actin were imaged during the reformation of junctional belts. ZO1 and F-actin
770    colocalize during elongation of the junctional condensates. Right panel: Reformation of junction
after calcium switch showed similar dynamics as the LatA switch.
(C) Quantification of the elongation speed of individual condensates from the in vitro experiments
shown in figure 4 and the LatA and Ca switch experiments. Elongation rates have a median of 0.5
± 0.2 μm/min for in vitro experiments, 0.5 ± 0.1 μm/min for calcium switch and 0.6 ± 0.3 μm/min
775    for the LatA switch.
(D) Model of tight junction belt assembly based on the experimental and theoretical results. ZO1
is recruited to cell-cell adhesion sites, by binding to oligomeric receptors. Multivalent interaction
of ZO1 drives surface condensation which induces partitioning of receptors and cortical proteins

27

including actin. ZO1 condensates facilitate local actin-polymerization, which drives elongation of
780    condensates and results in coalescence into continuous junctional belts.
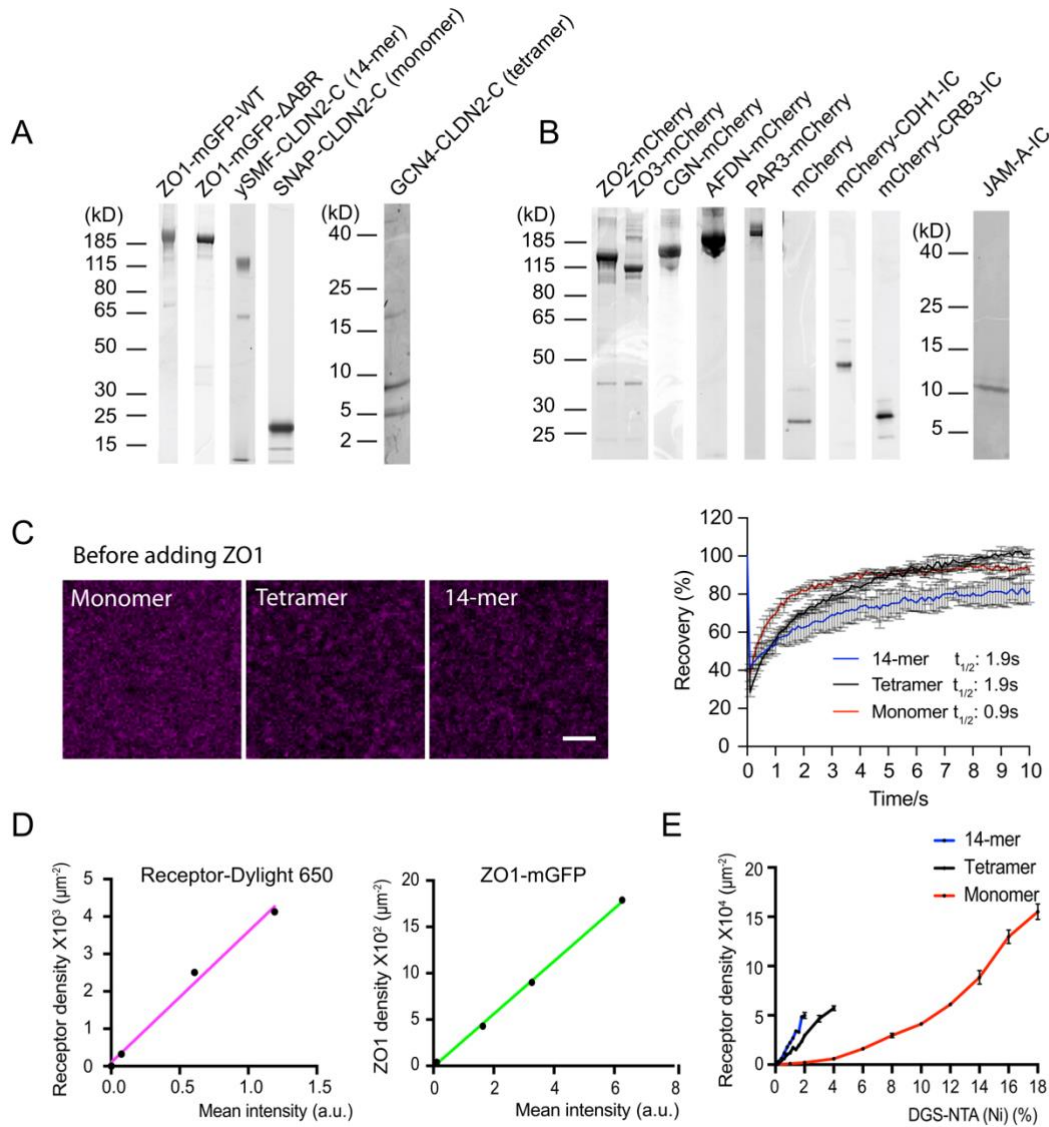
**Fig. S1. Receptors are dynamic before adding ZO1.** Related to Figure 1.

(A) Left: SDS-PAGE gel (stained with Coomassie blue) of ZO1-mGFP-WT, ZO1-mGFP-ΔABR, ySMF-CLDN2-C (14-meric receptor) and SNAP-CLDN2-C (monomeric receptor) proteins used in this study. Right: Tricine gel (stained with Coomassie blue) of GCN4-CLDN2-C (Tetrameric receptor) protein used in this study.

(B) Left: SDS-PAGE gel (stained with Coomassie blue) of mCherry tagged ZO2, ZO3, CGN, AFDN, PAR3, CDH1-IC, CRB3-IC and mCherry protein used in the partition assay. Right: Tricine gel (stained with Coomassie blue) of JAM-A-IC protein used in the partition assay.

(C) Left: Images of membranes functionalized with increasing amounts of monomeric, tetrameric, and 14-meric receptors. Receptors are all labeled with Dylight650. Right: Quantification of FRAP results of indicated receptors on membrane before adding ZO1. Values shown are the mean ± SD

795    from 3 independent measurements. A one phase association fitting was performed to get the half-time of recovery. Half-times of recovery after photobleach are annotated.

(D) Left: Calibration curve of Dylight650 labeled receptors. The X-axis shows the mean fluorescence intensity acquired from confocal images; The Y-axis shows the molecules/$\mu$m$^2$ from FCS measurement. The calibration equation is $Y = 3501*X + 97.29$. Receptor numbers are in the

800    unit of monomer. Right: Calibration curve of ZO1-mGFP. The X-axis shows the mean fluorescence intensity acquired from confocal images; The Y-axis shows the molecules/$\mu$m$^2$ from FCS measurement. The calibration equation is $Y = 284.4*X - 8.990$. ZO1-mGFP is in the unit of monomer.

(E) Quantification of indicated receptor densities with the increase of DGS-NTA(Ni) lipids on

805    membranes. Receptor densities were converted to molecules/$\mu$m$^2$ from fluorescence intensity with the calibration curve in (D). Values shown are the mean ± SD from three different views.
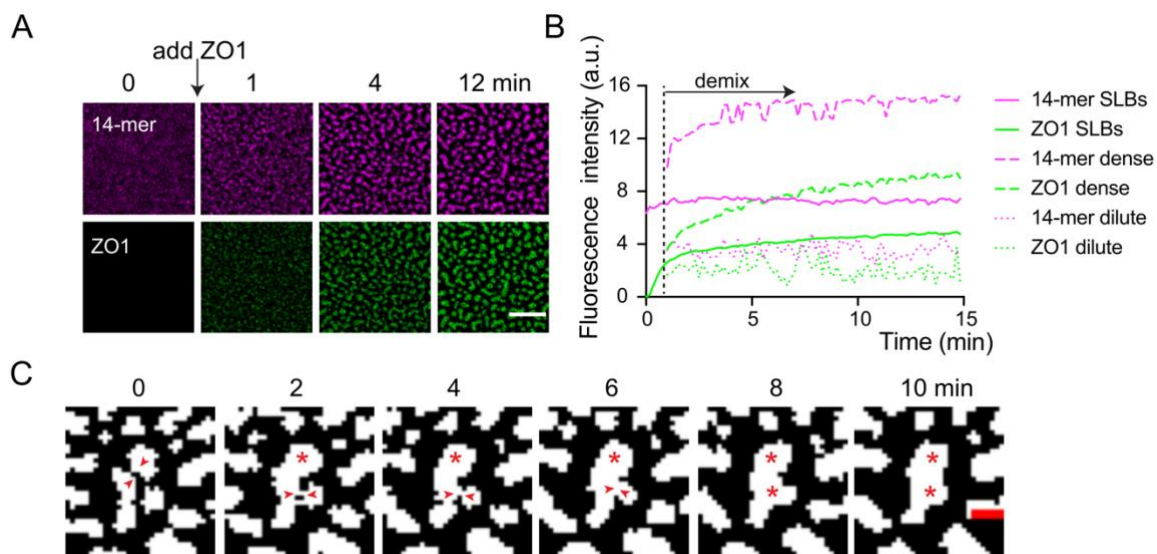
**Fig. S2. ZO1 surface condensates have liquid-like properties.** Related to Figure 1.

(A) Time series of ZO1 surface binding and condensation. 200 nM ZO1 was added to the membrane functionalized with 1400 molecules/µm2 14-mer-Dylight 650. Images were taken every 10 s for 15 min. Scale bar, 5 µm.

(B) ZO1 and 14-mer fluorescence signal quantification on whole membrane, in dense phase and in dilute phase form the time series in (A). Demixing of the bound ZO1 to form dense and dilute phases is annotated.

(C) Fusion events during ZO1 surface condensation with 14-mer receptors. The arrowheads show the droplets before fusion, the stars show the fused droplets. Scale bar, 2 µm.
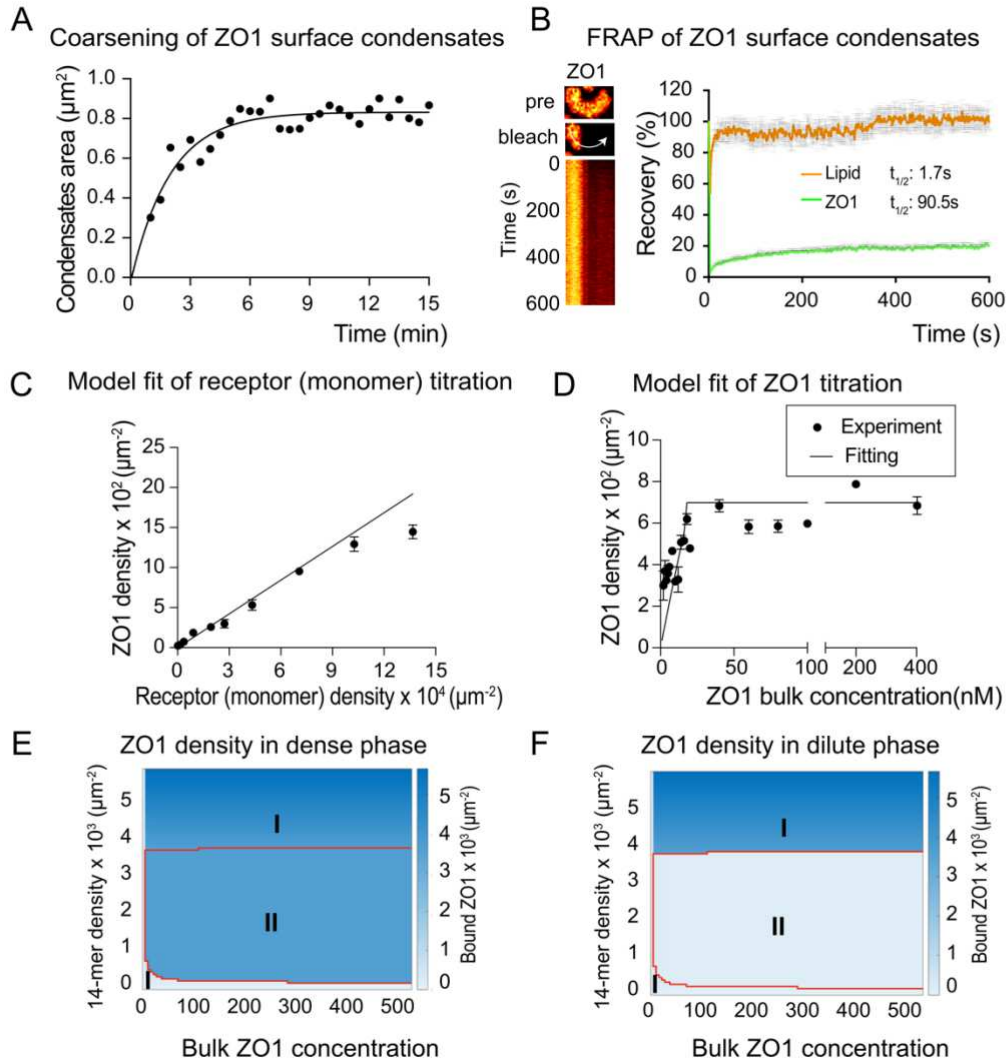
**Fig. S3. Fitting result of ZO1 membrane binding with monomer.** Related to Figure 2.

(A) Quantification of area change of ZO1 surface condensates after adding ZO1 from movie S1. A one phase association fitting was performed.

(B) Quantification of FRAP results of ZO1 surface condensates formed with 14-mer receptors. Kymograph of the recovery of ZO1 signal is shown on the left. Values shown are the mean ± SD from 3 independent measurements. A one phase association fitting was performed to get the half-time of recovery. Half-times of recovery after photobleach are annotated.

(C) Quantification of ZO1 density on the membrane from simulation and experiment when titrating the monomer receptor densities. Values shown are the mean ± SD from three different views.

(D) Quantification of ZO1 density on the membrane from simulation and experiment when titrating the ZO1 bulk concentration with monomer receptors on the membrane. Values shown are the mean ± SD from three different views.

(E) Phase diagram of ZO1 density in dense phase with 14-mer receptors from simulation. Phase I shows the regime with mixed surface and mixed bulk. Phase II shows the regime with demixed surface and mixed bulk.

(F) Phase diagram of ZO1 density in dilute phase with 14-mer receptors from simulation. Phase I shows the regime with mixed surface and mixed bulk. Phase II shows the regime with demixed surface and mixed bulk.

835
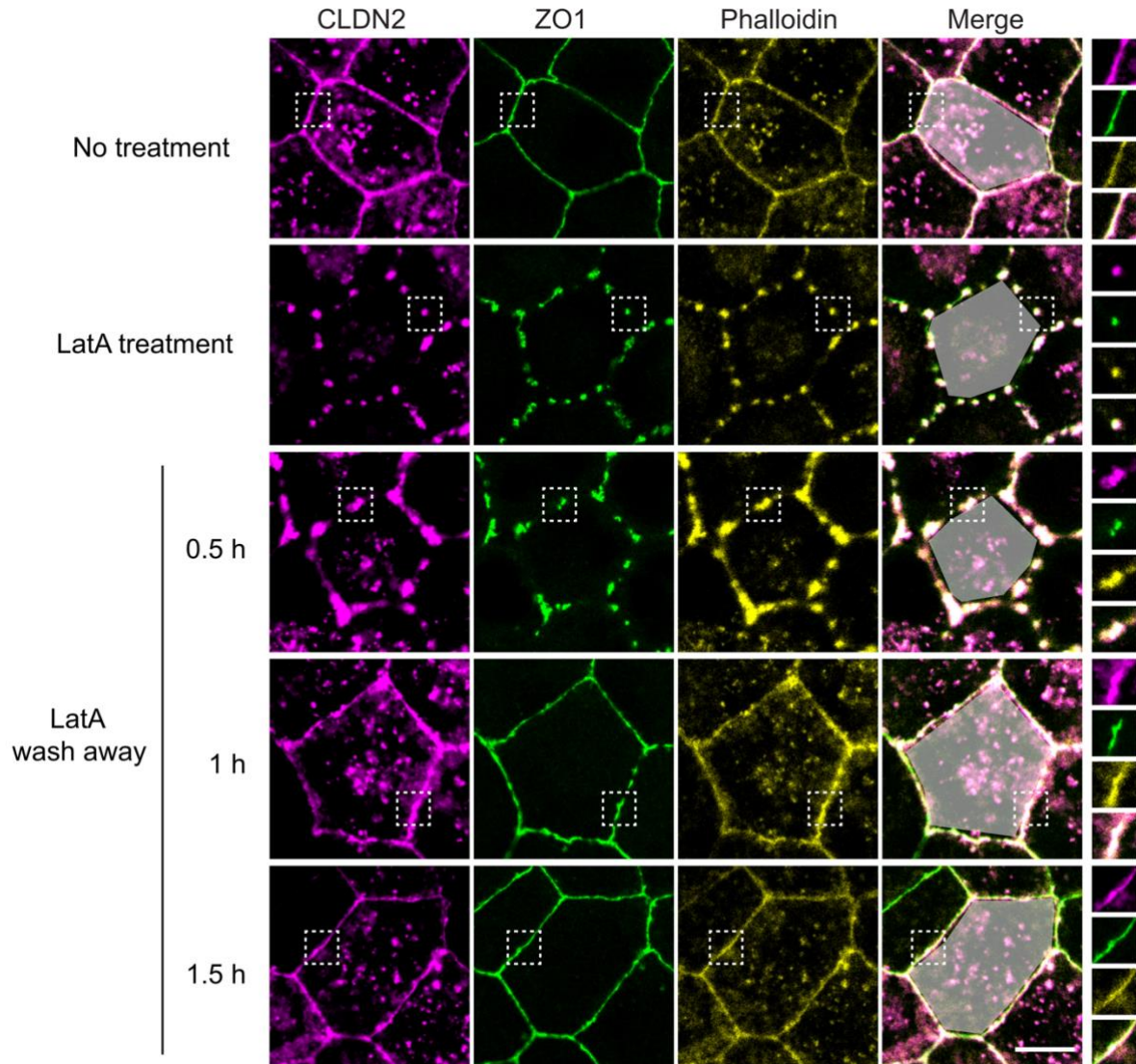
**Fig. S4. Tight junction belt formation correlates with actin elongation.** Related to figure 4. Confocal images of MDCKII monolayers with and without the treatment of Latrunculin A (LatA). Endogenous ZO1 was visualized via fusion NeoGreen (NG). CLDN2 was visualized with Halo-tagged CLDN2. F-actin was visualized with phalloidin staining. Colocalization of ZO1, CLDN2, and F-actin was evident during the elongation of tight junction belt. Zoom in images of tight junction condensates were shown on the right side. Scale bar, 10 µm.

840

845
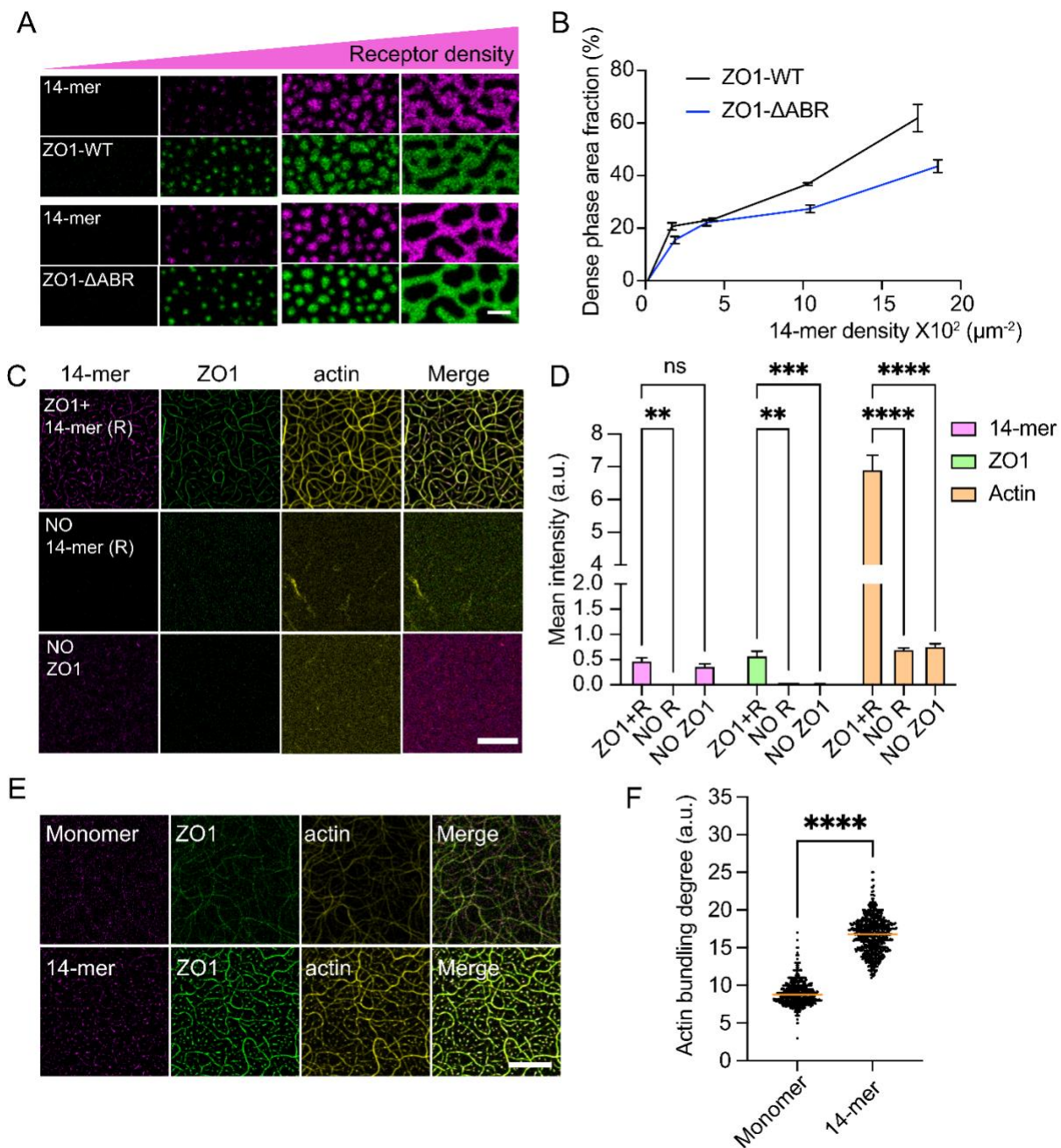
**Fig. S5. ZO1 surface condensates are vital for local actin polymerization.** Related to figure 4.
(A) Images of ZO1 surface condensates formed with ZO1-WT and ZO1-ΔABR. ZO1 surface condensates were formed by adding 200 nM ZO1-WT or ZO1-ΔABR to membranes functionalized with different amounts of 14-mer receptors. Scale bar, 2 µm.
(B) Dense phase area fraction quantification of ZO1 surface condensates from images in (A). Values shown are the mean ± SD from three different views.
(C) Actin local polymerization assay without ZO1 or 14-mer receptors. Scale bar, 10 µm.

(D) Quantification of ZO1, 14-mer receptor, and actin signal on the membrane from the images in (C). Values shown are the mean ± SD from 3 different views. A 2wayANOVA test was performed to determine the significance of the difference between different conditions.

(E) Actin polymerization assay with monomer or 14-mer on the membrane. 200 nM ZO1 protein was added to the membrane functionalized with similar amounts of monomer (~3900 molecules/$\mu$m$^2$) or 14-mer (~260 molecules/$\mu$m$^2$) for 10 min. Images were taken at 60 min after adding 3 uM G-actin-Alexa Fluor 647. Scale bar, 10 $\mu$m.

(F) Actin bundling degree quantification from the images in (E). Values shown are the mean ± SD from three different views. An ordinary one-way ANOVA was performed to determine the significance of the difference between monomer and 14-mer.
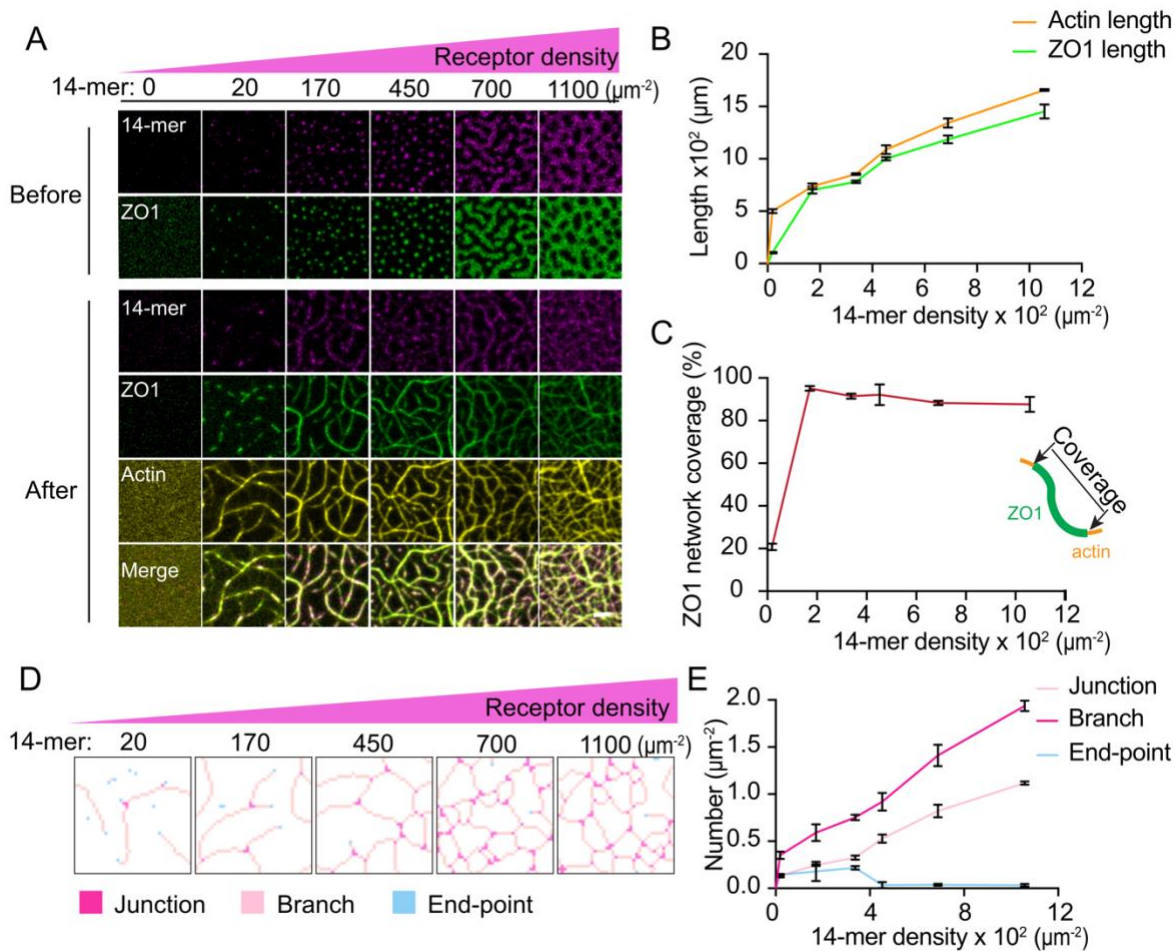
865

**Fig. S6. Tight junction connectivity and complexity depend on receptor density.** Related to Figure 4.

(A) Before: Images of ZO1 surface condensates formed with 14-mer receptors. ZO1 membrane condensates were formed by adding 200 nM ZO1 protein to membranes functionalized with

870   different amounts of 14-mer-Dylight 550 receptors. 14-mer receptor densities were annotated on the top. After: Images of tight junction like networks after adding 3 uM G-actin-Alexa Fluor 647 to ZO1 membrane condensates for 3 hrs. Scale bar, 2 µm.

(B) Network length quantification from ZO1 and actin signal after adding 3 uM G-actin-Alexa Fluor 647 to ZO1 surface condensates for 3 hrs from images in (A). Values shown are the mean ±

875   SD from three different views.

(C) Quantification of coverage degree of ZO1 network on actin networks from (B). Values shown are the mean ± SD from three different views.

(D) Network complexity analysis by skeletonizing actin networks from the images in (A) with Skeletonize Plugin in FIJI (https://imagej.net/plugins/skeletonize3d). The skeleton is classified

880   into end-point (less than 2 neighbors), branch (exactly 2 neighbors) and junction (more than 2 neighbors) by the number of neighbors.

(E) Quantification of network complexity from the skeletonized actin network in (D). Values shown are the mean ± SD from three different views.

## REFERENCES

1. Zihni, C., Mills, C., Matter, K. & Balda, M.S. Tight junctions: from simple barriers to multifunctional molecular gates. *Nat Rev Mol Cell Biol* **17**, 564-580 (2016).
2. Anderson, J.M. & Van Itallie, C.M. Physiology and function of the tight junction. *Cold Spring Harb Perspect Biol* **1**, a002584 (2009).
3. Citi, S. Intestinal barriers protect against disease. *Science* **359**, 1097-1098 (2018).
4. Beutel, O., Maraspini, R., Pombo-Garcia, K., Martin-Lemaitre, C. & Honigmann, A. Phase Separation of Zonula Occludens Proteins Drives Formation of Tight Junctions. *Cell* **179**, 923-+ (2019).
5. Umeda, K. *et al.* ZO-1 and ZO-2 independently determine where claudins are polymerized in tight-junction strand formation. *Cell* **126**, 741-754 (2006).
6. Schwayer, C. *et al.* Mechanosensation of Tight Junctions Depends on ZO-1 Phase Separation and Flow. *Cell* **179**, 937-952 e918 (2019).
7. Brangwynne, C.P. *et al.* Germline P Granules Are Liquid Droplets That Localize by Controlled Dissolution/Condensation. *Science* **324**, 1729-1732 (2009).
8. Patel, A. *et al.* A Liquid-to-Solid Phase Transition of the ALS Protein FUS Accelerated by Disease Mutation. *Cell* **162**, 1066-1077 (2015).
9. Sun, D., Wu, R., Zheng, J., Li, P. & Yu, L. Polyubiquitin chain-induced p62 phase separation drives autophagic cargo segregation. *Cell Res* **28**, 405-415 (2018).
10. Brangwynne, C.P., Mitchison, T.J. & Hyman, A.A. Active liquid-like behavior of nucleoli determines their size and shape in Xenopus laevis oocytes. *P Natl Acad Sci USA* **108**, 4334-4339 (2011).
11. Boija, A. *et al.* Transcription Factors Activate Genes through the Phase-Separation Capacity of Their Activation Domains. *Cell* **175**, 1842-+ (2018).
12. Fritsch, A.W. *et al.* Local thermodynamics govern formation and dissolution of Caenorhabditis elegans P granule condensates. *Proc Natl Acad Sci U S A* **118** (2021).
13. Hyman, A.A., Weber, C.A. & Julicher, F. Liquid-liquid phase separation in biology. *Annu Rev Cell Dev Biol* **30**, 39-58 (2014).
14. Su, X. *et al.* Phase separation of signaling molecules promotes T cell receptor signal transduction. *Science* **352**, 595-599 (2016).
15. Zeng, M. *et al.* Reconstituted Postsynaptic Density as a Molecular Platform for Understanding Synapse Formation and Plasticity. *Cell* **174**, 1172-1187 e1116 (2018).
16. Wang, Y. *et al.* LIMD1 phase separation contributes to cellular mechanics and durotaxis by regulating focal adhesion dynamics in response to force. *Dev Cell* **56**, 1313-1325 e1317 (2021).
17. Degennes, P.G. Wetting - Statics and Dynamics. *Rev Mod Phys* **57**, 827-863 (1985).
18. Cahn, J.W. Critical-Point Wetting. *J Chem Phys* **66**, 3667-3672 (1977).
19. Rutledge, J.E. & Taborek, P. Prewetting Phase-Diagram of He-4 on Cesium. *Phys Rev Lett* **69**, 937-940 (1992).
20. Chandavarkar, S., Geertman, R.M. & Dejeu, W.H. Observation of a Prewetting Transition during Surface Melting of Caprolactam. *Phys Rev Lett* **69**, 2384-2387 (1992).
21. Kellay, H., Bonn, D. & Meunier, J. Prewetting in a Binary-Liquid Mixture. *Phys Rev Lett* **71**, 2607-2610 (1993).
22. Zhao, X.P., Bartolucci, G., Honigmann, A., Julicher, F. & Weber, C.A. Thermodynamics of wetting, prewetting and surface phase transitions with surface binding. *New J Phys* **23** (2021).

23. Morin, J.A. *et al.* Sequence-dependent surface condensation of a pioneer transcription factor on DNA. *Nature Physics* **18**, 271-+ (2022).

24. Quail, T. *et al.* Force generation by protein-DNA co-condensation. *Nature Physics* **17**, 1007-+ (2021).

25. Sasaki, H. *et al.* Dynamic behavior of paired claudin strands within apposing plasma membranes. *P Natl Acad Sci USA* **100**, 3971-3976 (2003).

26. Zhao, J. *et al.* Multiple claudin-claudin cis interfaces are required for tight junction strand formation and inherent flexibility. *Communications Biology* **1** (2018).

27. Liu, J. *et al.* Conformational specificity of the Lac repressor coiled-coil tetramerization domain. *Biochemistry-Us* **46**, 14951-14959 (2007).

28. Collins, B.M. *et al.* Homomeric ring assemblies of eukaryotic Sm proteins have affinity for both RNA and DNA - Crystal structure of an oligomeric complex of yeast SmF. *Journal of Biological Chemistry* **278**, 17291-17298 (2003).

29. Erlendsson, S. *et al.* Mechanisms of PDZ domain scaffold assembly illuminated by use of supported cell membrane sheets. *Elife* **8** (2019).

30. Ebnet, K., Schulz, C.U., Meyer Zu Brickwedde, M.K., Pendl, G.G. & Vestweber, D. Junctional adhesion molecule interacts with the PDZ domain-containing proteins AF-6 and ZO-1. *J Biol Chem* **275**, 27979-27988 (2000).

31. Rouaud, F. *et al.* Scaffolding proteins of vertebrate apical junctions: structure, functions and biophysics. *Biochim Biophys Acta Biomembr* **1862**, 183399 (2020).

32. Shin, K., Straight, S. & Margolis, B. PATJ regulates tight junction formation and polarity in mammalian epithelial cells. *J Cell Biol* **168**, 705-711 (2005).

33. Sasaki, K. *et al.* Shank2 Binds to aPKC and Controls Tight Junction Formation with Rap1 Signaling during Establishment of Epithelial Cell Polarity. *Cell Reports* **31** (2020).

34. Wang, Q. & Margolis, B. Apical junctional complexes and cell polarity. *Kidney Int* **72**, 1448-1458 (2007).

35. Citi, S. The mechanobiology of tight junctions. *Biophys Rev* **11**, 783-793 (2019).

36. Belardi, B. *et al.* A Weak Link with Actin Organizes Tight Junctions to Control Epithelial Permeability. *Dev Cell* **54**, 792-804 e797 (2020).

37. Kuhn, J.R. & Pollard, T.D. Real-time measurements of actin filament polymerization by total internal reflection fluorescence microscopy. *Biophys J* **88**, 1387-1402 (2005).

38. Melak, M., Plessner, M. & Grosse, R. Actin visualization at a glance. *Journal of Cell Science* **130**, 525-530 (2017).

39. Otani, T. *et al.* Claudins and JAM-A coordinately regulate tight junction formation and epithelial polarity. *J Cell Biol* **218**, 3372-3396 (2019).

40. Gonschior, H. *et al.* Nanoscale segregation of channel and barrier claudins enables paracellular ion flux. *Nat Commun* **13**, 4985 (2022).

41. Case, L.B., De Pasquale, M., Henry, L. & Rosen, M.K. Synergistic phase separation of two pathways promotes integrin clustering and nascent adhesion formation. *Elife* **11** (2022).

42. Pombo-García, K., Martin-Lemaitre, C. & Honigmann, A. (2022).

43. Odenwald, M.A. *et al.* The scaffolding protein ZO-1 coordinates actomyosin and epithelial apical specializations in vitro and in vivo. *J Biol Chem* **293**, 17317-17335 (2018).

44. Cordenonsi, M. *et al.* Cingulin contains globular and coiled-coil domains and interacts with ZO-1, ZO-2, ZO-3, and myosin. *J Cell Biol* **147**, 1569-1582 (1999).

45. Paschoud, S., Guillemot, L. & Citi, S. Distinct domains of paracingulin are involved in its targeting to the actin cytoskeleton and regulation of apical junction assembly. *J Biol Chem* **287**, 13159-13169 (2012).

46. Yan, V.T., Narayanan, A., Wiegand, T., Julicher, F. & Grill, S.W. A condensate dynamic instability orchestrates actomyosin cortex activation. *Nature* **609**, 597-604 (2022).

47. Yuan, F. *et al.* Membrane bending by protein phase separation. *Proc Natl Acad Sci U S A* **118** (2021).
48. Sun, H., Luo, Y. & Miao, Y. Purification of Globular Actin from Rabbit Muscle and Pyrene Fluorescent Assays to Investigate Actin Dynamics in vitro. *Bio Protoc* **8**, e3102 (2018).
985 49. Swoboda, M. *et al.* Enzymatic Oxygen Scavenging for Photostability without pH Drop in Single-Molecule Experiments. *Acs Nano* **6**, 6364-6369 (2012).

# Supplementary Files

This is a list of supplementary files associated with this preprint. Click to download.

- SupplementaryInformationModellingSunetal.pdf
- MovieS1.avi
- MovieS2.avi
- MovieS3.avi